Quantifying coastal cliff retreat using *Structure-from-Motion* photogrammetry in the Minas Basin, Nova Scotia

by

Ian Hay

Submitted in partial fulfillment of the requirements

for the degree of Master of Science

at

Dalhousie University

Halifax, Nova Scotia

July 2020

For Mom and Dad

And if California slides into the Ocean
Like the mystics and statistics say it will,
I believe this hotel will be standing
Until I pay my bill.
                -Warren Zevon

Table of Contents:

List of Tables:

List of Figures:

Abstract:

Rates of retreat of cliffed coastlines are increasing around the globe, but the causes of observed increases are unclear. Lack of understanding complicates assessment of the risks to coastal infrastructure associated with rising sea levels. The frequencies and magnitudes of the coastal cliff erosion events that combine to produce overall, longer-term rates of retreat historically have been poorly constrained because observations generally were not possible on the time scales associated with major terrestrial and oceanographic forcings, which include, among others, heavy precipitation, repeated freeze-thaw cycles, and large waves associated with high water levels. To address mis-match between observational time scales and time scales of event-driven erosion, a two-part study is undertaken. In the first part, analysis of archived aerial photographs is used to produce approximately decadal estimates of coastal retreat over the past 8 decades at Thomas' Cove Coastal Reserve in Economy, Nova Scotia. In the second part, Structure-from-Motion (SfM) analysis is used to survey actively eroding cliffs at Thomas' Cove. On multiple visits between June 2018 and October 2019, photographs were taken with a camera mounted on a small Remotely Piloted Aircraft (sRPA). Images are used to create three-dimensional point-clouds, Digital Surface Models (DSMs) and orthomosaics with Pix4D, a commercially available SfM software package. DSMs and orthomosaics are used to map the position of the cliff top through the observation period. Calculated short-term retreat rates are compared to decadal-scale retreat rates for Thomas Cove determined from archived aerial photos and previous studies in the area. These rates indicate that present retreat rates are statistically similar to long-term averages and higher than rates observed over the past four decades. Additionally, volume change is calculated using GIS techniques and found to be consistent with values calculated in the same region by Wilson et al, 2017.

Acknowledgements:

Chapter 1

Introduction:

Cliffed shorelines comprise between 52 and 80% of the global coastline (Young and Carilli, 2018; Emery and Kuhn, 1982) and play important roles in ecosystems by providing sediment to adjacent coastal areas (Brooks and Spencer, 2010; Trenhaile, 2016; Wilson et al., 2016), and as habitat for wildlife and plants (Cooper, 1997; McCorquodale, et al., 2004; Ancillotto et al., 2014). Coastal cliffs can fail rapidly, which threatens coastal communities (Paone, 2003; Marques et al., 2011) and infrastructure (Stavrou et al., 2011) and can cause injury and loss of life (Maxouris, 2019). These risks are being exacerbated worldwide by increasing rates of coastal retreat due to elevated rates of sea level rise (Brown et al., 2014; Wong et al., 2014).

The Minas Basin in the uppermost reaches of the Bay of Fundy in Atlantic Canada is fringed by large sections of high cliffs composed of friable sandstone and unconsolidated glacial till, making it an excellent location to study rates and mechanisms of cliff retreat. The cliffs of the Minas Basin are eroding rapidly, with average retreat rates of 0.5 m a^{-1} (Wilson et al., 2017). Retreat rates of this magnitude pose problems for infrastructure around the Basin. For example, a map extrapolating retreat rates calculated by Wilson et al., 2017 out to the years 2100 and 2200 shows the extent of damage to infrastructure and personal property to be expected along a small stretch of coastline in the coming centuries if rates of retreat remain stable (Fig. 1.1).
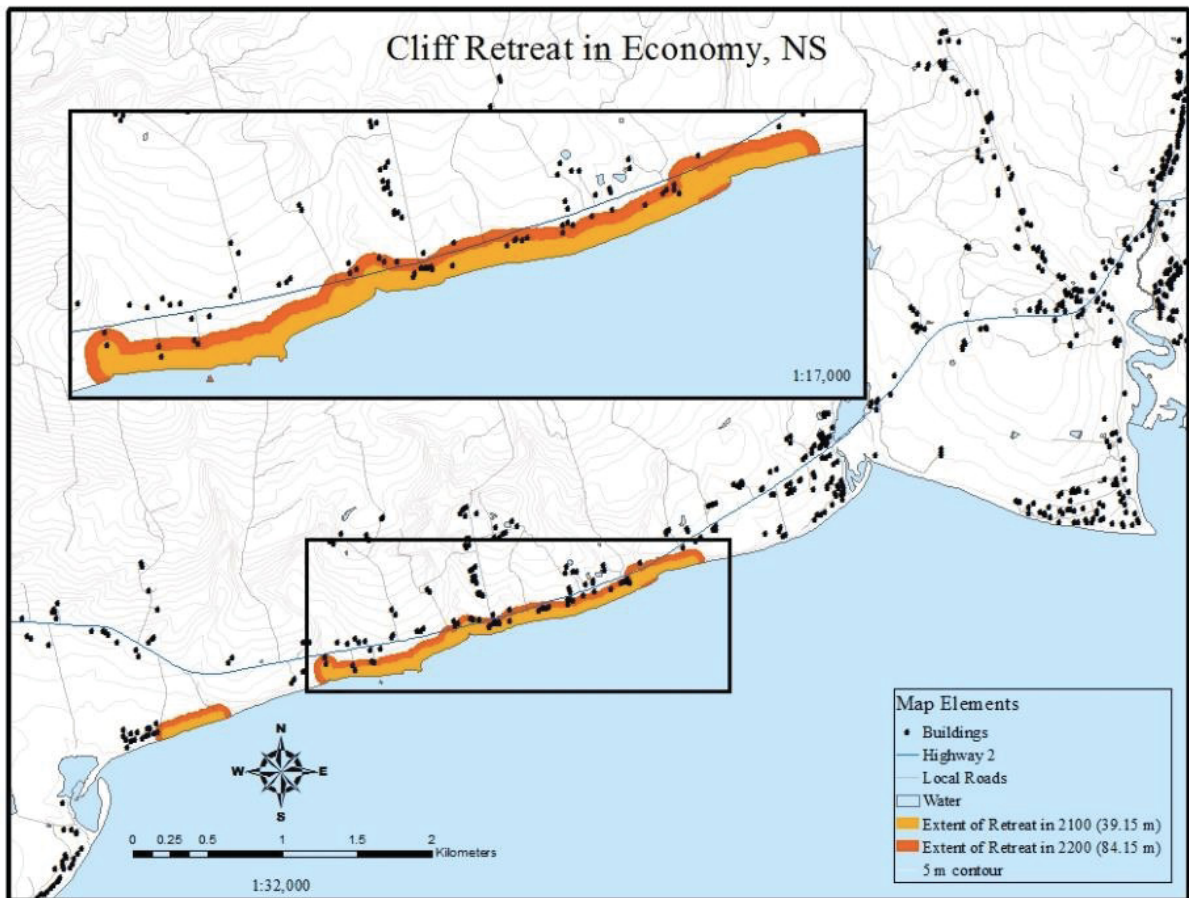
Figure 1.1: Local projected cliff retreat in Lower Economy, Colchester County, Nova Scotia. The highlighted box indicates an area with many houses and a long stretch of the Glooscap Trail (NS Route 2) at risk from destruction by cliff failure in the next century. Erosion rates in this section are estimated at 0.45 m/yr according to Wilson, 2016.

Historically, studies of coastal cliff retreat have relied on aerial surveys for determining long-term retreat rates and on direct physical measurements for investigating retreat over shorter time scales (Paone et al., 2003, Bernatchez and Dubois, 2008, Garae, 2015). The use of historic air photos is limited to analysis of 20 year or longer time-spans due to the high levels of uncertainty associated with poor spatial resolution in the imagery. Because of this low temporal resolution, the role of episodic erosion events on long-term averages is not well-resolved in studies using historic air photos. Direct physical measurements can be highly accurate and allow for high-temporal resolution estimates of retreat but are labor-intensive and are typically limited to measurements of a single feature (i.e. changes in cliff break position) on a given day. For example, Garae (2015) investigated retreat of several cliffed coastlines around Tauranga Harbour in New Zealand using air photos from 1943, 1982 and 2011. She found that annual retreat rates were roughly 0.2 m/yr, attributing differences in retreat to lithology. Bernatchez and Dubois (2008) studied retreat rate of a fine-grained cliff on the north shore of the Saint Lawrence estuary in Quebec between 1998 and 2003 by making direct measurements of cliff edge location relative to stakes driven into the top of the cliff. They found that average annual retreat increased from 1 m/yr in 1999-2000 to 1.7 m/yr in all following years. Bernatchez and Dubois (2008) attributed 65% of total erosion to the winter season, and they identified ice expansion within joints as the primary cause of block failure.

The rate of coastal retreat in the Minas Basin of the Bay of Fundy in Nova Scotia estimated by analysis of aerial photographs increased by ~25% during a period extending from the early 1990s to 2013 relative to a period extending from the mid-1960s to the

early 1990s (Wilson et al., 2017). The causes of increased coastal retreat rate were not resolved by Wilson et al., 2017, primarily because the goal of that study was to develop synoptic estimates of coastal retreat across the entire Minas Basin. This goal limited analysis to the time periods for which there was complete coverage of the Minas Basin with aerial photographs. The resulting low, ~25-year temporal resolution did not support analysis of the correlation between retreat rates and the terrestrial and oceanographic variables that drive coastal erosion. The use of small Remotely Piloted Aircraft (sRPAs) (commonly referred to as "drones") for coastal monitoring was a logical extension from existing aerial survey programs utilizing piloted aircraft such as the California Coastal Records Project (Adelman & Adelman, 2019). sRPAs allow for rapid acquisition of coastal imagery at relatively low cost compared with other platforms and can be flown with fewer airspace restrictions than apply to conventional manned aircraft. Additionally, sRPAs can be flown at low altitudes providing valuable information on the cliff face. The goal of this study is to provide a detailed comparison of long-term and short-term retreat rates by using conventional and emerging survey technologies to estimate retreat rates, combined with local measurements of sea level to help elucidate possible relationships between tidal activity and material removal from the cliff toe at various locations along the cliff.

Chapter 2

Methodology:

2.1 Study Area:

The Minas Basin experiences some of the largest tidal ranges on Earth. In 1998 a 16.3-metre difference between high water level and next low water level was measured at Burntcoat Head on the southern shore of the Basin, and the predicted maximum tidal range over the period of 1998-2016 was 17.0 metres (O'Reilly et al., 2005). With each ebb and flood of tide, roughly 3 billion cubic meters of water pass through Minas Passage between the Basin and the Bay of Fundy, more than the total outflow of all the world's rivers, twice a day (Parker et al., 2007).

This study focuses on Thomas' Cove Coastal Reserve in Economy, Nova Scotia on the north shore of the Central Minas Basin (Fig. 2.1). Thomas' Cove falls within an area identified as having the highest rates of coastal cliff retreat in the Minas Basin (~0.5 m/yr) (Wilson et al., 2017). The main cliff face at Thomas' Cove is oriented perpendicular to the direction of mean westerly winds and southwesterly swell and thus provides insight into the role that waves play in erosion. The relatively unconsolidated sandstones and glacial tills that lie along the coast at Thomas' Cove are found throughout the Minas Basin and they are of similar composition as other rapidly eroding coastlines around the world.

Logistically, the study site is located in Class G airspace allowing operation of the sRPA without risk of interference with structures on shore or active commercial airspace, as prescribed by Transport Canada. Given three hours on either side of high tide, the exposed beach provides a broad, flat landing zone where the sRPA can be safely launched and landed.

This study site is covered by aerial photos covering a span of 80 years. Such a long record allows identification of trends in cliff retreat at Thomas' Cove, and these findings inform risk assessment and retreat analysis in other parts of the Minas Basin.
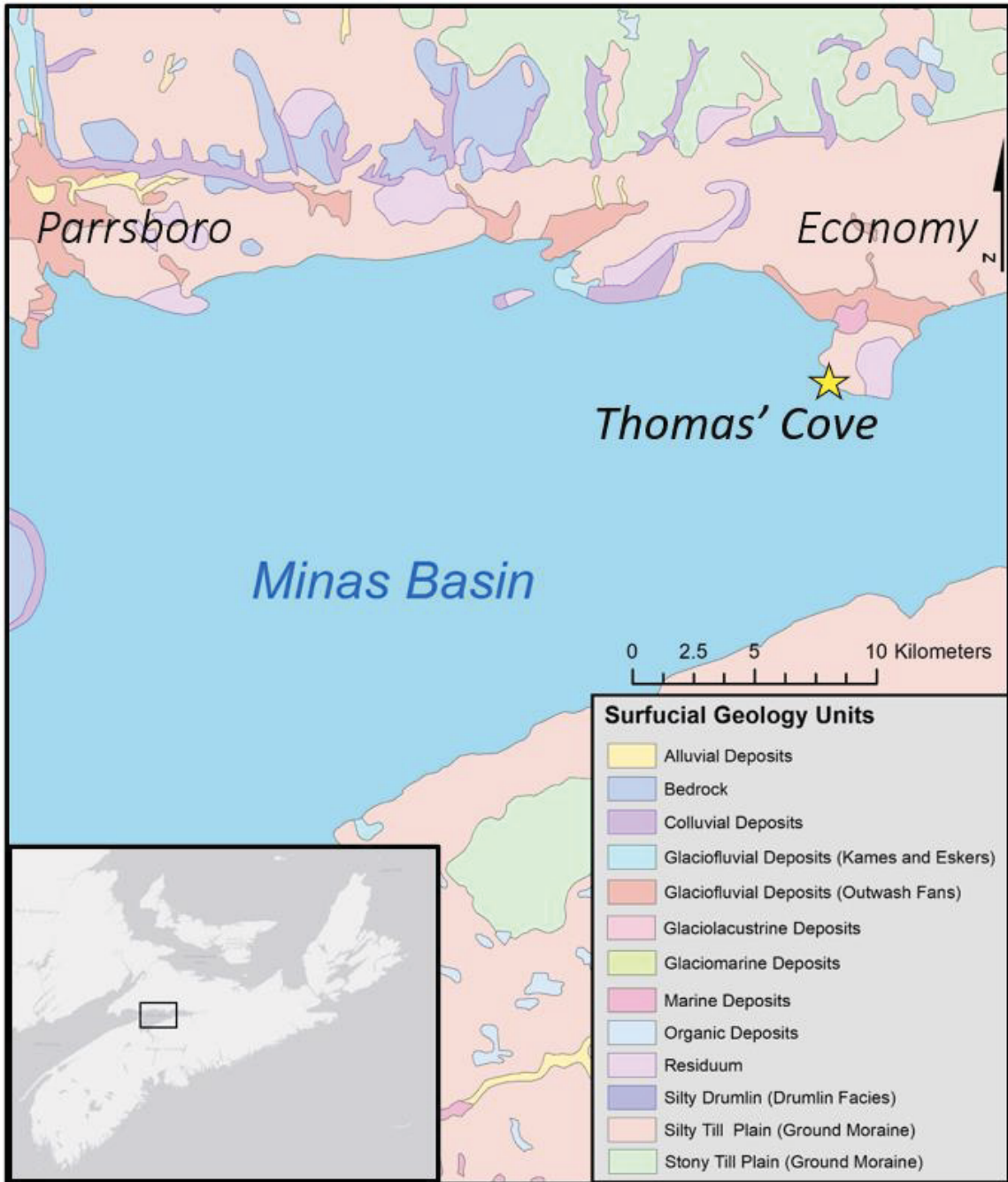
Figure 2.1: Study area at Thomas Cove Coastal Reserve along the north shore of the Central Minas Basin between the communities of Parrsboro and Economy, with surficial geology units.

2.1.1 Geology:

The Minas Basin formed when rivers that were eroding eastward along the Bay of Fundy scoured a channel along the Minas Passage Fault between Cape Split and Cape Sharp. The basin also has been reshaped by a series of glaciations (Parker et al., 2007). The cliffs along the north shore of the Central Minas Basin are primarily composed of Jurassic and Triassic sandstones of the Wolfville and Horton Bluff formations (Colwell & Ferguson, 1992; Kettanah et al., 2013), their red color derived from the presence of oxidized iron-rich hematites (Parker et al., 2007). Initially, sands deposited in the Triassic Lowlands, at a time when the land that is now Nova Scotia was still part of Pangea. The sands were deposited by rivers and winds into a tectonic basin surrounded by mountains. The deposits were later altered during glaciations that have left a thick silty till plain comprised of loosely consolidated sediment with a wide range of particle sizes on top of the sandstone cliffs.

2.2 Historic air photo analysis and retreat rates:

Aerial photographs were obtained for fourteen dates from 9 different years between 1938 to 2007 (Table 1). Images were obtained from the National Air Photo Library (NAPL) in Ottawa and from the Nova Scotia Geomatics Centre in Amherst, Nova Scotia. Following the same techniques employed by Wilson et al., 2017, high-quality digital scans of these images were digitally orthorectified and used to calculate decadal retreat rates based on the position of the cliff break.

Table 1: air photos obtained from the National Air Photo Library in Ottawa and the Nova Scotia Geomatics Centre in Amherst, NS. Not all photos were used directly for analysis, but most were considered for visual inspection of cliff-top features.

Year	Date	Number of frames	Source
1938	19-May	6	NAPL
1948	16-May & 23-Jun	4	NAPL
1954	14-Jul	2	NAPL
1959	5-Jun	4	NAPL
1969	15-Oct	2	NAPL
1972	23-May	2	NAPL
1979	23-May & 15-Jul	4	NAPL
1994	5-Jun	6	NS Geomatics Centre
2007	NA	2	NS Geomatics Centre

Air photos were georeferenced using the georeference toolbar within ArcGIS Pro. Up to five ground control points were added to each image at clearly visible road intersections, field boundaries, and in some instances, river channels. Before georeferencing began, image spatial reference was set to UTM WGS 1984 zone 20 North, with vertical reference to the Canadian Geodetic Vertical Datum of 2013 (CGVD2013), the same spatial reference used throughout this study. The initial image (1938) was georeferenced against the provided imagery base-layer in ArcGIS Pro. All following images were georeferenced against the baselayer and checked against the

preceding image using the swipe tool. Georectification was carried out using an affine 1st order polynomial transformation. Total root mean squared (RMS) error and residual errors associated with individual ground control points were recorded (Table 2). The total RMS error was later used in the analysis of decadal shoreline retreat rates.

Figure 2.2: Study site is circled in the bottom left of the frame. The position of 5 control points are shown over an image from 1938. These control points were used for georeferencing the historic air photo against features still clearly visible from modern aerial imagery, such as road intersections and field corners. Notice that the 5 control points are all located to the east of the cliff and are roughly collinear.

Once all airphotos had been georeferenced, the best were selected to be used for shoreline generation. Because of lens distortion, high surface reflectivity and shadow, not all images from the available years were suitable for further analysis. Moreover, the cliff break was used as the position from which retreat rates were calculated for all photos, but

it was not visible in some images due to glare, overhanging vegetation or blurriness in imagery. Shorelines were drawn by hand as polylines in ArcMap 10.5 and exported as shapefiles, again preserving the spatial reference information of the associated photograph.

The Digital Shoreline Analysis System (DSAS) produced by the U.S. Geological Survey (USGS) was used to estimate retreat rate of the shoreline (Himelstoss et al., 2018). DSAS casts an array of transects that are orthogonal to the shoreline shapefiles. The baseline for the transects was placed 10 meters from the earliest shoreline in the historic air photos, with a smoothing distance of 25 meters. Transects were placed every 10 meters along the length of the baseline. These parameters reduced the frequency of transects "missing" shorelines around headlands or other convoluted features. The date and uncertainty associated with each photo were used to calculate rates of change of shoreline position. The specifics of this technique can be found in the DSAS users guide (Himmelstoss et al., 2018).

2.3 Structure from Motion (SfM):

Structure from Motion photogrammetry (SfM) is a technique used to create 3-dimensional point clouds from a series of overlapping photographs taken from different locations (Fig. 2.3.1). The technique can be accurate to sub-centimeter scale, and it is used extensively in construction, commercial surveying, and resource management (e.g., Caroti et al., 2015, Micheletti et al., 2015). The technique has also been used to study coastal cliff environments and mass-wasting events along sea cliffs (Stavrou et al., 2011; Ruzic et al., 2014; Warrick et al., 2018), coastal dunes (Mancini et al., 2013), and

agricultural drainage ditches (Prostocini, et al. 2015). There are several commercially-available and open-source software programs for SfM. Pix4D was selected because of its reputation as being user-friendly and intuitive. After collecting photographs in the field, the software extracts the camera's metadata, including GPS position. The software identifies common points in overlapping photographs and performs a series of triangulations on these points to construct a 3-dimensional surface. Spatial reference marks called Ground Control Points (GCPs) are also used to accurately pin the 3-dimensional surface to the Earth.
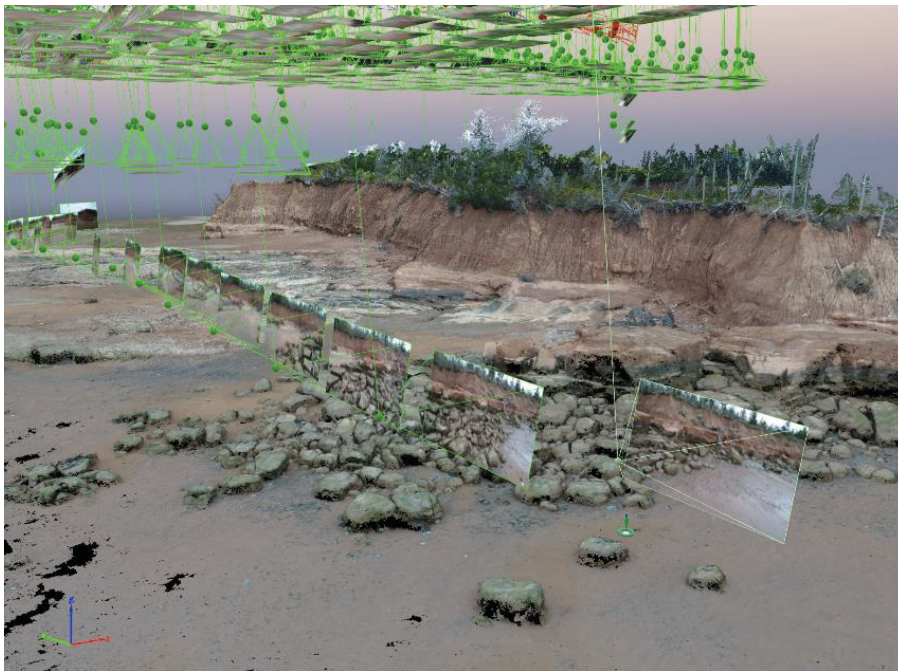
Figure 2.3.1: Screen capture from a Pix4D model showing the many camera angles used for reconstruction of a dense 3-dimensional point cloud. Green dots represent the point from which each photo was taken with the image itself shown in front normal to the angle and attitude at which it was captured.

SfM is capable of generating accurate digital surface models (DSMs) which can be used within a mapping package such as ArcGIS to investigate cliff motion along the x and y axes, with similar accuracy to the considerably more expensive technologies of terrestrial laser scanning and light detection and ranging (LiDAR) (Shürch et al., 2011, Lague et al., 2013, Warrick et al., 2017) (Fig. 2.3.2).
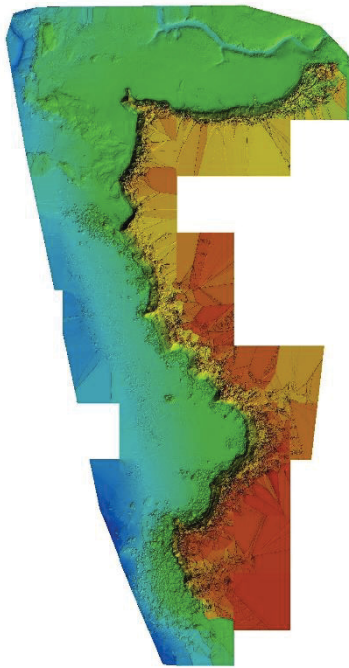
Figure 2.3.2: Digital Surface Model (DSM) of study area.

SfM provides oblique 3D projections which permits investigations of cliff modification that may occur in overhanging sections otherwise not visible from a traditional nadir projection (Ruzic et al., 2014). Additionally, Pix4D produces an orthorectified photo mosaic (from here on 'orthomosaic'), which can be used in a similar way as historic air photos, where the cliff break is traced within a GIS software.

2.4 Site surveying and ground control points:

Construction of accurate digital models of land surfaces with Structure-from-Motion technology requires multiple ground control points (GCPs) in the survey region. These GCPs ideally are surveyed with the cm-scale accuracy available with Real Time Kinematic (RTK) GPS technology. RTK GPS surveys employ a base station and a rover station that receives positional corrections from the base station. For this research, a Hemisphere S320 Base and Rover RTK unit were used in concert with Carlson SurvCE software loaded onto an accompanying Windows phone. For the 2018 surveys the RTK base station was placed at the same location for each survey, and it was allowed to calculate its position each time based on available GPS satellites. This technique produced base station positions with ± ~0.5 m accuracy, which clearly was not adequate to resolve changes in the position of the shoreline. In 2019 a new survey strategy was implemented, in which the base station was placed at the same location for each survey, and it was provided with that location with cm-scale accuracy. To establish the position of the base station, raw GPS data were collected for 2 hours, and these data were submitted to Natural Resources Canada (https://webapp.geod.nrcan.gc.ca/geod/tools-outils/ppp.php) to establish Precise Point Positioning (PPP) of the base station location.

A localization file for the area was established with a two-point localization. Localization is a way of transforming the geoid surface of a small area on Earth to a planar surface, allowing for simpler calculation of positions in XYZ space. Two points were surveyed in with raw GPS data and PPP processing. One point was used to adjust the vertical position of the planar surface, and the two points together were used to adjust the horizontal position of the planar surface. To check RTK GPS accuracy before each

survey, the reported position of a check point was compared to its previously determined PPP location. Deviations between measured x and y locations and the PPP locations less than 2.5 cm and deviation between measured z location and PPP z location less than 5 cm were deemed acceptable (Wisconsin Department of Transportation, 2017). All precisely positioned points are ground features in rock platforms; three were naturally-occurring boreholes and, one was a petroglyph (fig. 2.4.1).

The positions of GCPs for the first three 2018 surveys were collected using the earlier methodology that used a base station position determined during each survey. These surveys were corrected by shifting all GCP locations by the difference observed between the permanent clifftop GCPs using the average position of a GCP from all 2019 surveys. The Pix4D model was re-run with corrected ground control points and the location of independent check points (boreholes) were used to validate the corrections.

Figure 2.4.1: A) borehole used as a checkpoint on the south end of the cliff. B) same borehole as in panel A with bipod rover mast in place. C) large spiral petroglyph used as main localization point near the middle of the cliff. This feature, which is on top of a large outcrop that is easily accessible, is situated in the middle of the survey area both horizontally and vertically.

Surveying protocol is as follows:

1. Set up GPS Base following manufacturer's instructions at the elevation used when raw data was collected over that point, plumb above the precisely known base station point with antenna arm oriented to the same direction (this study used 161 degrees [magnetic]).

2. Set up GPS base and rover to the elevation used on all previous surveys

3. Load localization (.loc) file stored within the GPS handheld unit

4. Collect a position at the check point and evaluate output against PPP report from NRCAN

5. If any point is off by more than 5 cm, reload localization, check heights of base and rover antennae, and repeat.

Ground control points are reference marks of known position used to bring imagery or a model into alignment. Ground control points may be any points with known XYZ coordinate locations. These points may be in the form of an existing structure, survey target, or other immobile object. For this study, due largely to the dynamic nature of the study site (it becomes fully inundated by high tide), small portable targets were deployed and surveyed in using the RTK rover unit before the start of each mission. These were located on the intertidal cliff platform and along the top of the cliff. A combination of rectangular (61 x 49 cm) white Coroplast™ sheets with large black crosses painted on them and bucket lids (31 cm diameter) with 6-cm dots painted on their centers were used as temporary GCPs (Fig. 2.4.2). An additional five permanent GCPs made from bucket lids were placed along the cliff top so that they were visible from a downward-looking sRPA. They were fixed in place by dropping them onto the tops of 3-

foot lengths of ½ inch rebar pounded vertically into the ground until they were nearly flush with the ground.

Surveys were conducted in 2018 on June 7, July 19, and August 17, and in 2019 on June 25, September 20, and October 21. each survey was processed within Pix4D which produced a 3D point cloud, orthomosaic and digital elevation model (DEM).

Figure 2.4.2: Left: semi-permanent GCP in the form of a plastic bucket lid held in place with landscaping staples and ½ inch rebar near the cliff break. Right: Coroplast™ GCP target in place on the beach at Thomas Cove.

2.5 sRPA and Mission Planning:

A DJI Phantom 4 Advanced quadcopter sRPA was used to collect photographs at Thomas' Cove. Flight tracks were pre-programmed using Litchi Mission Hub (https://flylitchi.com/hub) run through an Apple iPad mini. Flights were designed to "scan" the study area from above and from the side. Oblique photographs provided information on the face of cliffs and in overhanging areas that nadir flights and satellite imagery would not capture. Because the cliff section lies roughly north-south, long passes were flown cross shore east-to-west at ~3 m/s separated by 10 meters north-to-south (Fig. 2.5), at an elevation of 50 meters with the camera pointed straight down. When a flight mission was started, the camera began taking photos automatically every five seconds, recording images in both raw and JPEG format. This flight path provided photos with roughly 80% overlap with frames adjacent on all sides, and a ground sampling distance (pixel size) of 1.4 cm. To compensate for the rolling shutter effect, the sRPA was instructed in the Litchi Mission Hub to pause and rotate by 90 degrees at each waypoint so that the camera would always face in the direction of travel. Unfortunately, the sRPA did not respond appropriately to this programming, instead executing in-flight turns. This unsolved flight programming issue prevented correction of the rolling shutter effect. Additional photos were captured of the cliff face from oblique flights flown at 10 meters with the camera pointing straight ahead and at 30 meters with the camera angled down at an angle of ~45°.
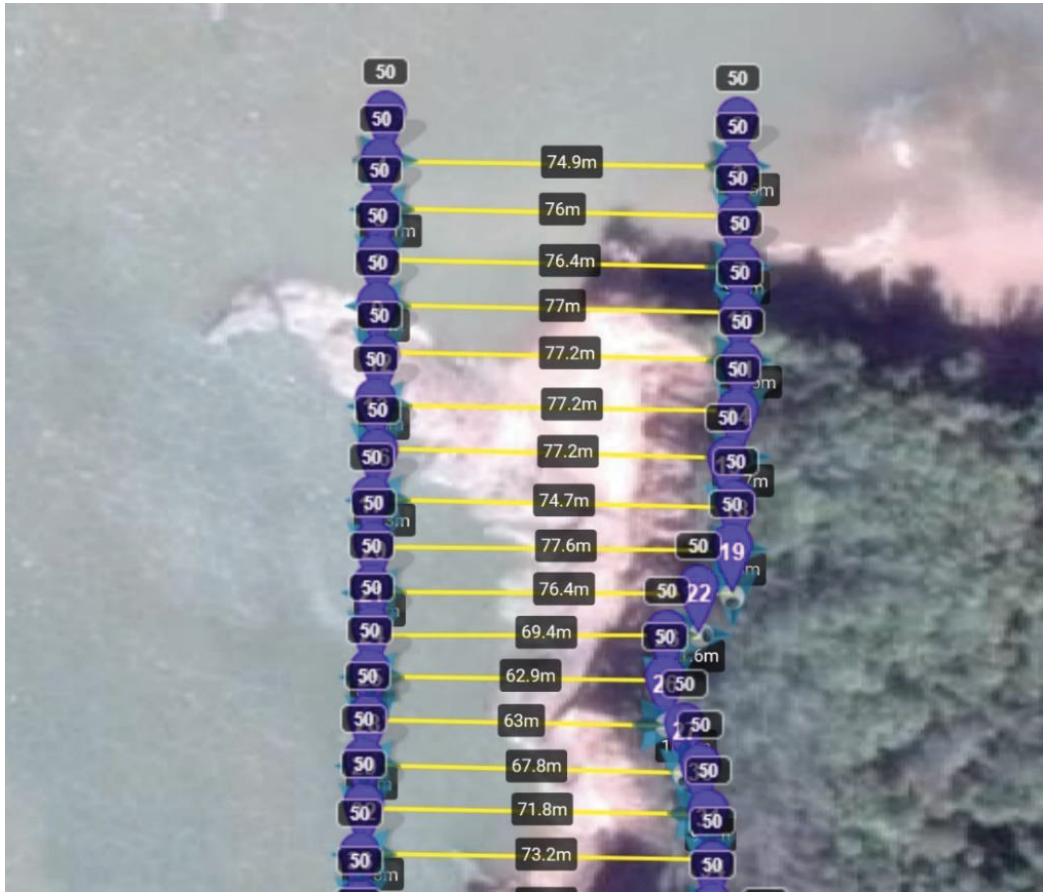
Figure 2.5: Screen capture of Litchi Mission Hub. Yellow lines represent the sRPA flight path with path length shown in shaded boxes.The purple pins are numbered waypoints at which the sRPA must change direction, with the elevation of the sRPA shown in the shaded box above them.

2.6 Retreat rates from SfM-derived photomosaics

Shorter interval retreat rates were determined from model-generated photomosaics from the sRPA surveys. Photomosaics were better for identification of the cliff-break (as indicated by the vegetation line) than the DSMs, because the edge of the till layer (which has been used as the cliff break for the historic air photos as well) can easily be misinterpreted as the edge of the sandstone layer beneath. A uniform smoothing distance of 10 meters was chosen with transects spaced every 5 meters along the baseline.

2.7 Uncertainty and Ground Sampling Distance

Three times the ground sampling distance (GSD) was used as uncertainty values for each shoreline air-photo shoreline (Table 2). As with the historic air photos, the uncertainty value for each orthomosaic-derived shoreline was calculated as three times the ground sampling distance for each date reported in the initial quality report in Pix4D (Table 3).

Table 2: uncertainty values associated with each years' shoreline. Root mean squared error or uncertainty values are generated during the georectification of air photos. Shaded rows indicate years that were used for shoreline change analysis.

Year	Ground Sampling Distance (GSD) (meters)	RMSE (meters)
1938	0.35	4.41
1948	0.72	4.49
1954	0.36	2.03
1959	1.22	1.52
1969	3.45	1.33
1972	0.55	2.70
1979	1.71	2.58
1994	0.42	2.67
2007	1.71	2.51
2013	1.00	NA

Table 3: Average ground sampling distance (GSD) and mean georeferencing RMS error for all 3D models used for shoreline change analysis. GSD is the length of one edge of a pixel while RMS error is the uncertainty associated with fitting the model to surveyed GCPs. Three times the GSD is the value used for reporting uncertainty in DSAS.

Date	Average GSD (m)	Error (3xGSD)	Georeferencing Mean RMSE (m)
6/7/2018	0.014	0.042	0.029
7/19/2018	0.013	0.040	0.028
8/17/2018	0.013	0.039	0.027
6/25/2019	0.015	0.046	0.015
9/20/2019	0.013	0.040	0.015
10/21/2019	0.013	0.040	0.017

2.8 Cliff volume measurements

Volumes of portions of the cliff face were extracted using the volumes tool within Pix4D, which provides the user with terrain 3D area (m^2), fill volume (m^3), cut volume (m^3), their associated errors, and the total volume error (m^3). In all instances, a polygon was drawn from just outside the cliff toe up to near the cliff break. The polygons were aligned with the lowest point (usually the seaward edge). Polygons were drawn based on visual interpretation of the cliff from repeat visits, and they represent an array of cliff morphologies seen throughout the entire cliff section (Fig. 2.8.1). The "Point" position located at the northernmost end of the cliff represents a steep, narrow headland overlain by a thick layer of till. The "Caves" are features directly to the south of the "Point" that are covered seasonally by slumping till from above, and that are excavated gradually over the course of several months. The "Slump" developed between November 1, 2018 and December 14, 2018 when a large portion of the cliff gave way and slumped approximately 1.5 meters down the face of the cliff. The final and southernmost polygon is the "Rockfall" site that encompasses the area around a sandstone headland from which

a massive boulder separated from the rest of the cliff during the spring of 2019. Inspection of the boulder on the 28th of May, 2019 revealed a young evergreen pinned beneath the boulder which still retained healthy green needles, indicating that the rockfall occurred recently.

Figure 2.8.1: Polygons used for volume calculation within Pix4D. Sites were selected based on visual observation of change and representation of typical shoreline features.

A second analysis was performed on the entire face of the cliff by combining the values

from three polygons drawn from the north end of the cliff to near the southernmost end

(Fig. 2.8.2).

Figure 2.8.2: Polygon used for calculating volume of entire cliff face within Pix4D.

2.9 Sea level and climate records:

To obtain local sea-level data an RBR solo 3 sub-surface pressure sensor was deployed in late June 2019 in the flats just south of the cliffs being investigated (Fig. 2.9). The location of the pressure sensor was surveyed using RTK GPS within the same localization as all GCPs so the height from which pressure sensor readings were taken could be compared to the height of the cliff toe at various points along the length of the cliff. Measurements were collected at a rate of 2 Hz from the 28th of June to the 30th of July, 2019 after which measurements were recorded every 5 minutes from the 31st of July onwards into December 2019, from which the mean M2 tidal constituent could be resolved.
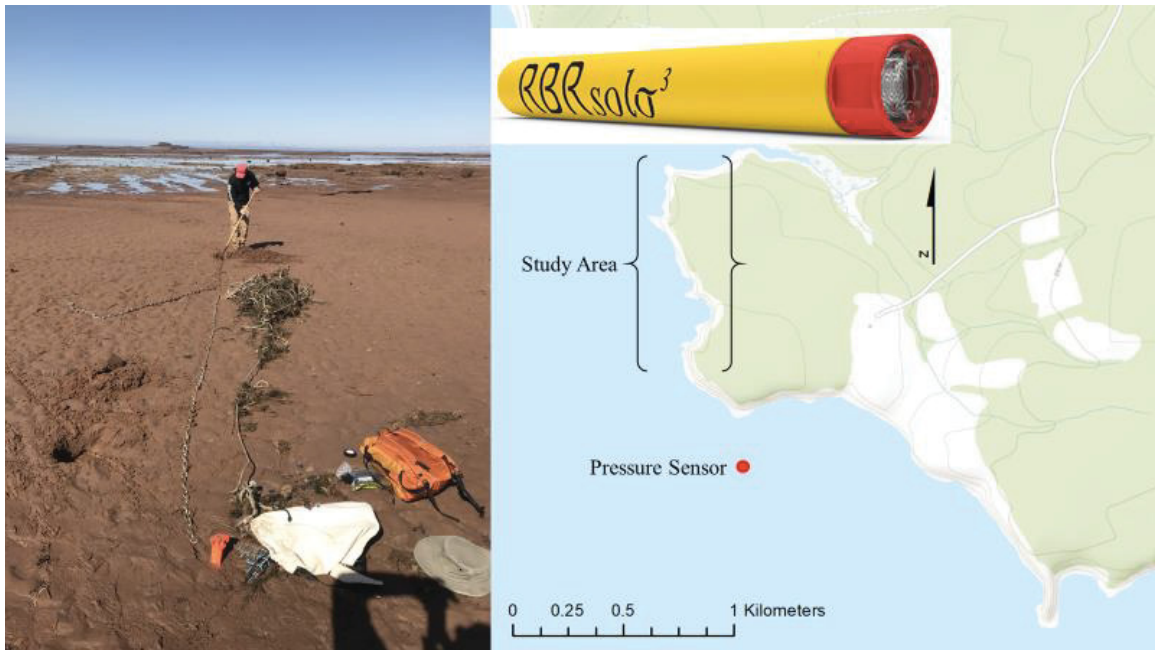
Figure 2.9: installation of RBR Solo 3 pressure sensor on the beach platform to the south of the study site cliffs. A 10-meter length of chain was attached to an orange survey stake near a pile of flotsam and pot warp attached to a buried lobster trap. The pressure sensor was installed vertically and wrapped with a piece of geotextile fabric secured with electrical tape. The position of the pressure sensor is indicated on the map by a red dot.

Chapter 3

Results:

3.1 Historic air photos and retreat rates:

In total, 5 shorelines were chosen for analysis: 1948, 1954, 1972, 1994, and 2013. Total

shoreline movement beginning in 1948 ranged from -118.29 meters to -8.66 meters of

retreat along the cliff over the 65-year period. For single-span rates, which is the rate of

change between two shorelines, the end-point rate (EPR) was calculated by dividing the

distance of the shoreline movement by the time elapsed between two shorelines.

Individual time spans were compared to one another to investigate seasonal variability.

The Kruskal-Wallis test was chosen after the Shapiro-Wilks test for normality showed

that none of the distributions were normal and closer investigation of histograms showed

a variety of distributions between date ranges, making a uniform normalizing

transformation of data impossible. The Kruskal-Wallis test is the non-parametric

equivalent of a one-way analysis of variance (ANOVA) and is used to evaluate whether

the medians of samples are different. The distribution of retreat values was in all years

predominantly left-skewed, and the spread of distributions decreased with time (Table 4).

Table 4: Distributions of End Point Rates (EPR) {m/yr} for periods spanning 1948-1954, 1954-1972, 1972-1994, and 1994-2013 with 10th, 25th, 50th, 75th, and 90th percentiles.

	10%	25%	50%	75%	90%
1948-1954	-4.70	-3.14	-1.38	-0.86	0.62
1954-1972	-0.91	-0.73	-0.51	-0.33	-0.20
1972-1994	-0.79	-0.63	-0.25	-0.07	-0.03
1994-2013	-0.54	-0.36	-0.20	-0.09	-0.05

Median retreat rates were progressively smaller from the mid-1900's through to 2013, with median retreat over the entire period ~1 m/a (Fig. 3.1.1)
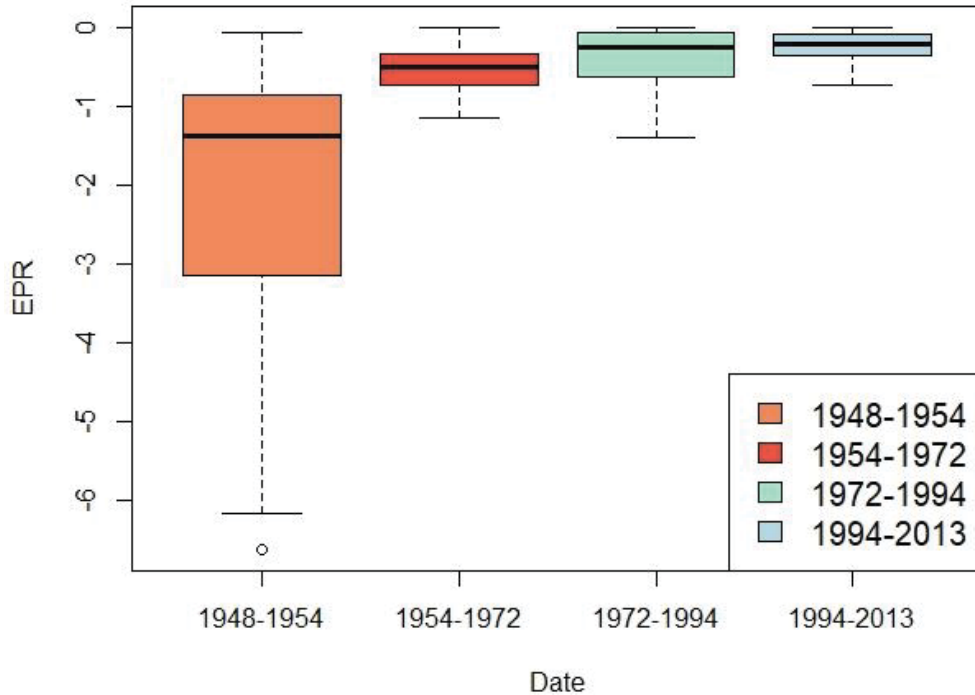
Figure 3.1.1: Box and whisker plot of End Point Rates (EPR) {m/yr} for periods spanning 1948-1954, 1954-1972, 1972-1994, and 1994-2013. The thick black line through each box represents the median and box edges are located at the 1st and 3rd quartiles. Whisker lines extend to 1.5x the interquartile range and points represent outliers.

Table 5 displays the results of comparing EPR values from all combinations of date ranges between 1948 and 2013. Of these combinations, only the last four decades (1972-1994 compared to 1994-2013) display a p-value greater than 0.05, suggesting that annual retreat was similar between 1972 and 2013. All other pairs rejected the null hypothesis with p-values well-below the 0.05 threshold.

Table 5: Comparison of end-point-rate (EPR) distributions between decadal periods using the Kruskal-Wallis test. Values <0.001 are reported as 0.000 and ≥0.05 highlighted in yellow.

	1948-1954	1954-1972	1972-1994	1994-2013
1948-1954	NA	0.00	0.00	0.00
1954-1972		NA	0.00	0.00
1972-1994			NA	0.14
1994-2013				NA

EPR was helpful for visualizing where retreat was most rapid along the cliff across all years (Fig. 3.1.2). Highest retreat was concentrated along the southern end of the cliff while low retreat rates dominated in the linear middle section.
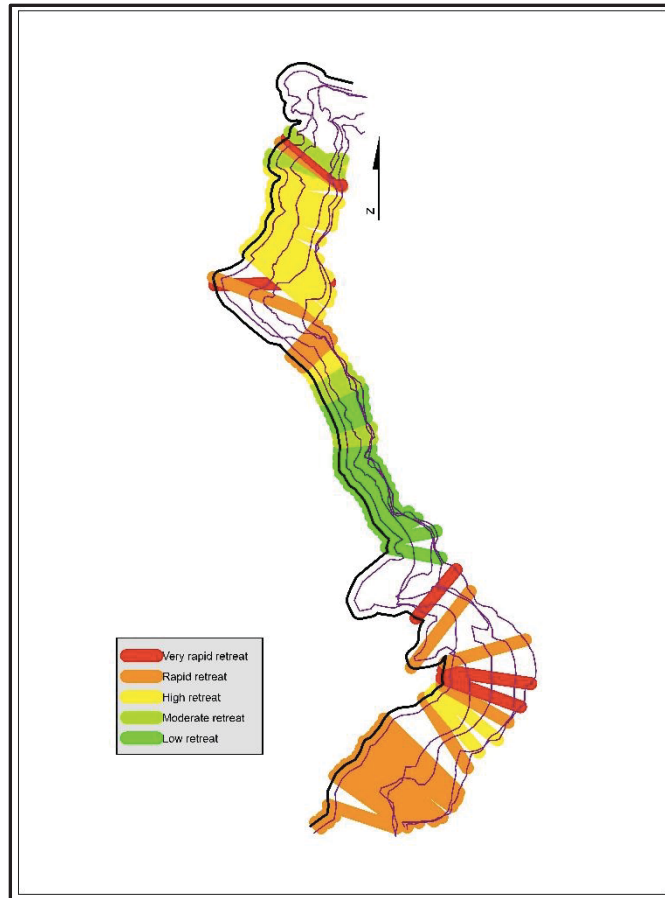
Figure 3.1.2: Transect plot showing areas with elevated retreat rates between 1948 and 2013. Hot colors indicate areas of high retreat while cool colors indicate lower retreat. Classifications are based on quintiles of EPR data. Sections of coastline between closely-spaced headlands and those facing the north-west have higher rates of retreat while the central linear section of cliff facing the south-west exhibit lower rates of retreat.

3.2 Retreat rates from SfM-derived orthomosaics

Net shoreline change between June 2018 and October 2019 ranged from -5.53 meters to -0.03 meters with a median long-term EPR of -0.57 m/yr. Highest median EPR was observed between June and July 2018 at -1.99 m/yr (Fig. 3.2) (Table 6).
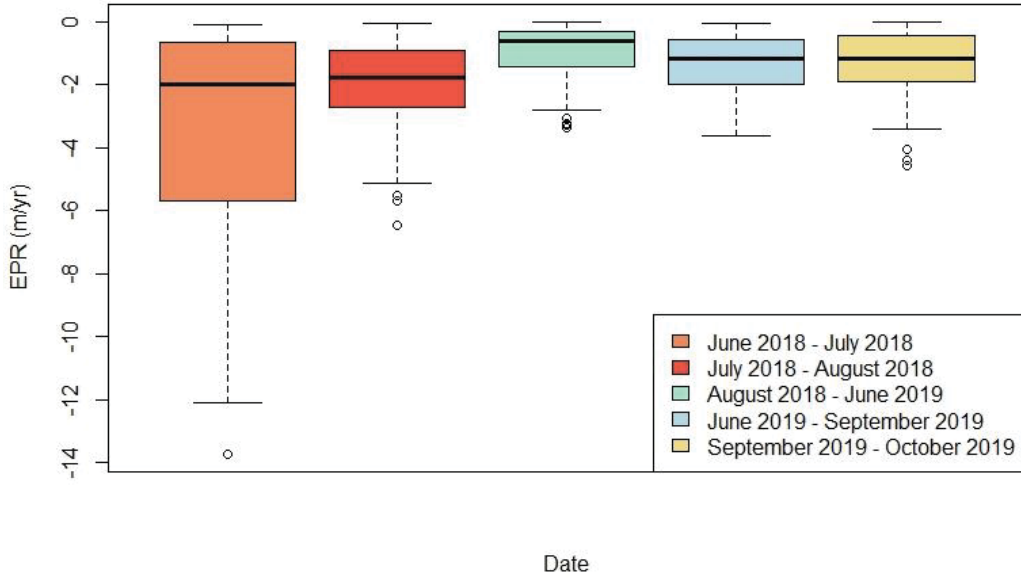
Figure 3.2: Box and whisker plot of End Point Rate (EPR) {m/yr} for periods spanning June 2018 to July 2018, July 2018 to August 2018, August 2018 to June 2019, June 2019 to September 2019, and September 2019 to October 2019.

As with the historic retreat rates, distributions were all left-skewed, and the widest distribution occurred between August, 2018 and June, 2019 (Table 6).

Table 6: Distributions of End Point Rates (EPR) {m/yr} for periods spanning June 2018 to July 2018, July 2018 to August 2018, August 2018 to June 2019, June 2019 to September 2019, and September 2019 to October 2019 with 10th, 25th, 50th, 75th, and 90th percentiles.

	10%	25%	50%	75%	90%
Jun 2018 - Jul 2018	-7.87	-5.62	-1.99	-0.65	-0.20
Jul 2018 - Aug 2018	-4.52	-2.71	-1.77	-0.90	-0.58
Aug 2018 - Jun 2019	-2.21	-1.41	-0.62	-0.32	-0.12
Jun 2019 - Sep 2019	-2.87	-1.99	-1.18	-0.58	-0.20
Sep 2019 - Oct 2019	-2.91	-1.88	-1.15	-0.45	-0.22

The two summer periods (June, 2018-July, 2018 compared to July, 2018-August, 2018 and June, 2019-September-2019 compared to September, 2019-October, 2019) were not statistically different from one another. However, the periods from June, 2018-July, 2018 and June, 2019-September, 2019 were statistically different from one another (Table 7). This suggests that retreat occurring during the 2018 and 2019 summer seasons are distinct from retreat occurring during the rest of the year, and that both summers experienced different rates of retreat. That all other combination of time periods rejected the null hypothesis supports the observation of lower retreat during Fall, Winter and Spring.

Table 7: Comparison of end-point-rate (EPR) distributions of monthly time periods using the Kruskal-Wallis test. P-values <0.001 are reported as 0.000, and ≥0.05 highlighted in yellow.

	Jun, 2018 - Jul, 2018	Jul, 2018 - Aug, 2018	Aug, 2018 - Jun, 2019	Jun, 2019 - Sep, 2019	Sep, 2019 - Oct, 2019
Jun, 2018 - Jul, 2018	NA	0.3170	0.000	0.0030	0.000
Jul, 2018 - Aug, 2018		NA	0.000	0.0060	0.0020
Aug, 2018 - Jun, 2019			NA	0.0090	0.0030
Jun, 2019 - Sep, 2019				NA	0.9870
Sep, 2019 - Oct, 2019					NA

3.2.1 Comparison of Modern and Historic retreat rates.

Mean estimates of long-term EPR based on recent surveys between June, 2018 and

October, 2019 was compared to individual time periods (Table 8). None of the monthly

periods show statistical similarity to the long-term EPR.

Table 8: Comparison of end-point-rate (EPR) distributions of long-term and decadal periods using the Kruskal-Wallis test. Values <0.001 are reported as 0.000.

EPR long-range (modern)	p (Kruskal - Wallis)
June, 2018 - October, 2019 v. June, 2018 - July, 2018	0.00
June, 2018 - October, 2019 v. July, 2018 - August, 2018	0.00
June, 2018 - October, 2019 v. August, 2018 - June, 2019	0.01
June, 2018 - October, 2019 v. June, 2019 - September, 2019	0.00
June, 2018 - October, 2019 v. September, 2019 - October, 2019	0.00

Comparisons were made between modern long-term retreat rates (June, 2018 to October,

2019) and both historic long-term (1948-2013, 1952-2013, etc.) and decadal rates, to

investigate if modern retreat rates are consistent with historic rates. Long-term retreat

rates from 1948-2013 and 1954-2013 were not statistically different from the 2018-2019

rates, but the 2018-2019 retreat rates were larger than the 1972-2013 and 1994-2013 rates

(Table 9).

Table 9: Comparison of end-point-rate (EPR) distributions of long-term (modern) and long-term (historic) using the Kruskal-Wallis test. Values <0.001 are reported as 0.000, and ≥0.05 highlighted in yellow.

EPR long-range (modern) v. EPR long-range (historic)	p (Kruskal - Wallis)
June, 2018 - October, 2019 v. 1948 - 2013	0.13
June, 2018 - October, 2019 v. 1954 - 2013	0.23
June, 2018 - October, 2019 v. 1972 - 2013	0.00
June, 2018 - October, 2019 v. 1994 - 2013	0.00

Historic long-term EPR values are statistically similar to those observed between June ,

2018 and October, 2019 from 1948 to 2013 and 1954 to 2013, with no significance for

later long-term rates. This suggests that modern retreat is similar to long-term retreat

observed over the past 65 years, but it is faster than the rates observed from 1972-1994

and 1994-2013 (Table 10).

Table 10: Comparison of end-point-rate (EPR) distributions of long-term (modern) and decadal (historic) using the Kruskal-Wallis test. Values <0.001 are reported as 0.000, and ≥0.05 highlighted in yellow.

EPR long-range (modern) v. EPR decadal (historic)	p (Kruskal - Wallis)
June, 2018 - October, 2019 v. 1948 - 1954	0.00
June, 2018 - October, 2019 v. 1954 - 1972	0.80
June, 2018 - October, 2019 v. 1972 - 1994	0.03
June, 2018 - October, 2019 v. 1994 - 2013	0.00

Only EPR values for the 1954-1972 time period show statistical similarity to the modern

long-term retreat values. In table 4 above, this same decadal period is dominant compared

to historic long-term retreat values. This result suggests that modern retreat is similar to

that observed between 1954 and 1972.

3.3 Cliff volume measurements

Cut volume decreased at all sites with rates ranging from -0.34 cubic meters of material per year (m^3/yr) at the Rockfall site to -0.06 m^3/yr at the Slump site (Fig. 3.3.1).
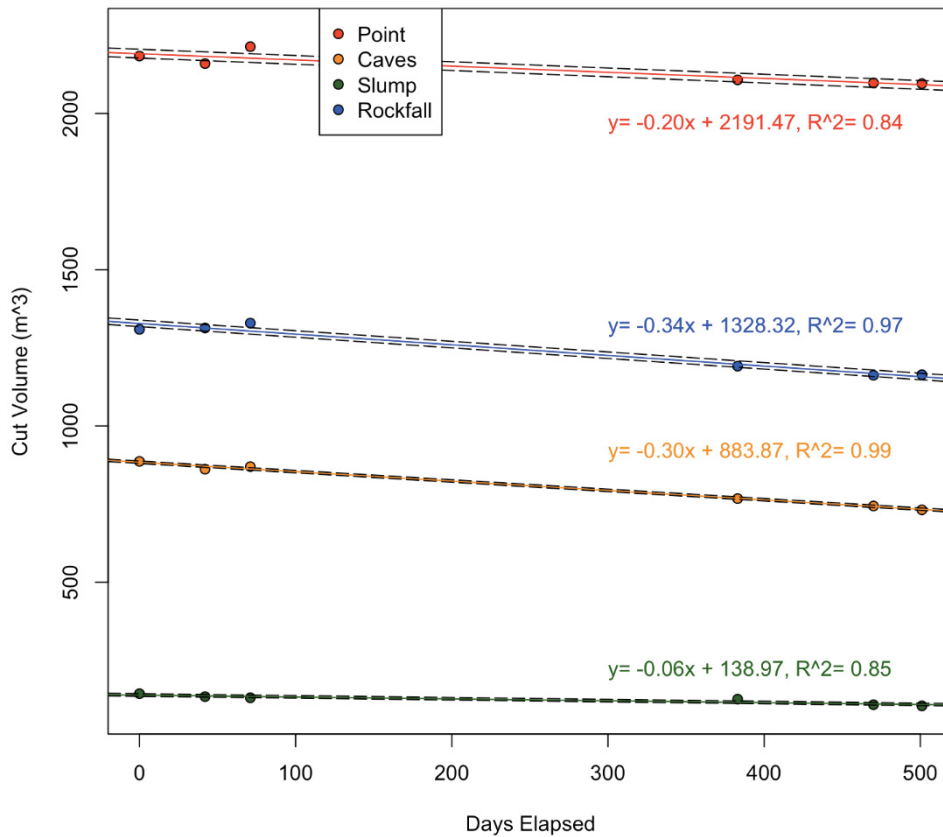
Figure 3.3.1: Cut volume of various features along the Thomas' Cove cliffs from 6/7/2018 to 10/21/2019. Measurements were made using the calculate volume tool within Pix4D. One standard error is shown as dashed lines above and below the regression lines for each site, with the equation for the line displayed directly above. Zero point on the x-axis represents 06/07/2018.

This analysis showed that total change in cut volume between July 2018 and October 2019 was -3296.5 m^3 ± 55.01 m^3. Over the sampling period of this study, the cliffs at Thomas' Cove lost material at a rate of 7.51 m^3/day, or 2741.15 m^3/yr (Fig. 3.3.2).
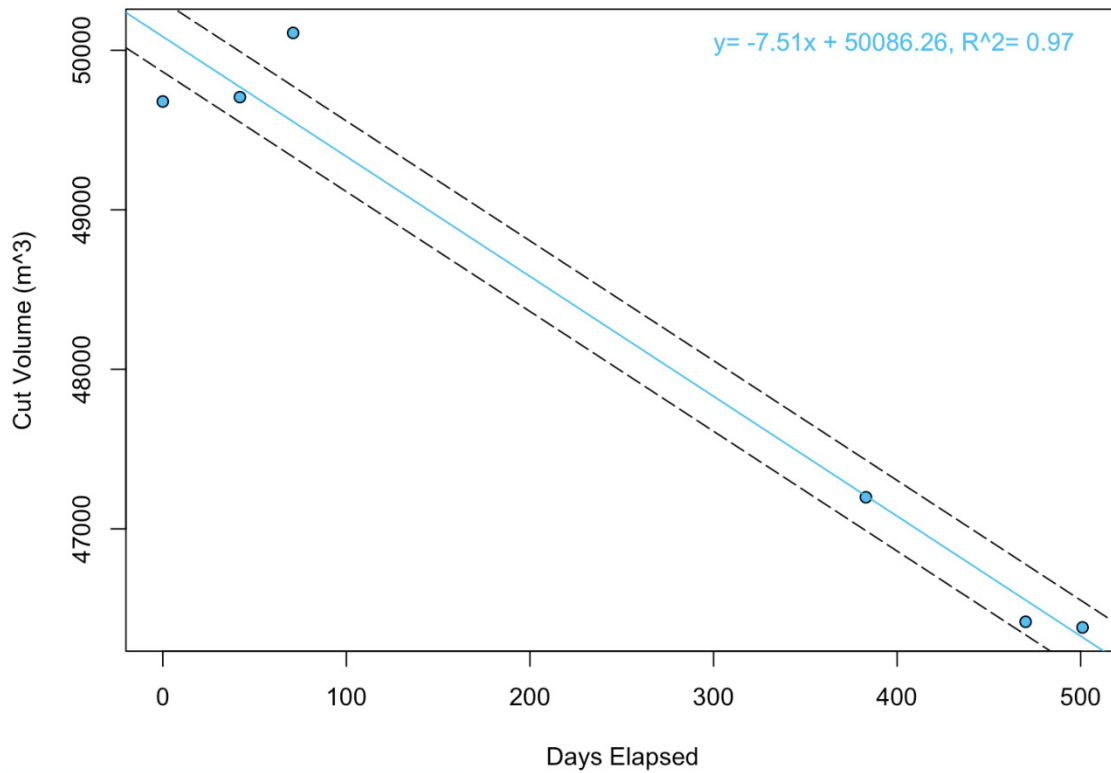

Figure 3.3.2: Cut volume of entire length of cliffs at Thomas' Cove. Measurements were made using the calculate volume tool within Pix4D. One standard error is shown in dashed lines above and below the intercept of the regression line. The regression line is describes by the equation in the top right of the figure.

Further analysis was performed to visualize the vertical change of the cliff face at each of the sample sites. The raster calculator was used to subtract the October 21, 2019 model DEM values from the June 7, 2018 model. Residuals were classified into five groups representing high erosion, moderate erosion, no change (between -10 and 10 cm of difference), moderate accretion and high accretion. Classified residuals were superimposed over the October 21, 2019 photomosaic extending to the position of the cliff break at that date (Figs. 3.3.3-3.3.5). Classifications were based on approximate quintiles of the data; -10 to 10 cm of change was classified as no change, 10-40 cm and -10 - -40 cm classified as moderate accretion and moderate erosion respectively and 40-100+ cm and -40 - -100+ cm classified as high accretion and high erosion, respectively.

At the "Caves and Headland" site an excavated talus slope is clearly visible directly beneath a large area of volume loss near the cliff break (Fig. 3.3.3). This talus slope was deposited before the June, 2018 survey and was entirely removed by October 2019. To the south of the Caves is a slump responsible for high erosion at the cliff top and accretion mid-cliff. To the north is a gully that is eroding material from near the cliff top and depositing material at the base.

The "Slump" site shows erosion across the entire cliff face with highest rates concentrated around the area of the rotational slump itself. Small accretionary talus slopes appear at the base of slump (Fig. 3.3.4). The image from October 21, 2019 shows that some of the trees attached to the former cliff-top are still upright, but undercutting has begun to compromise the platform of soil to which they are rooted.

At the "Rockfall" site, a large, multi-tiered rotational slump is framed by two large block failures on adjacent headlands (Fig. 3.3.5). The cuspate area between the two headlands

shows two accretionary talus slopes: one directly beneath the cliff break and a second at the cliff toe. The more northerly rockfall (closer to the top of the image) shows primarily material loss without a distinct talus surface, whereas the smaller rockfall on the southern headland has rotated down and away from its original position on the cliff face with new material clearly visible at the cliff toe. New boulders are visible at the base of the cliff in October 2019.
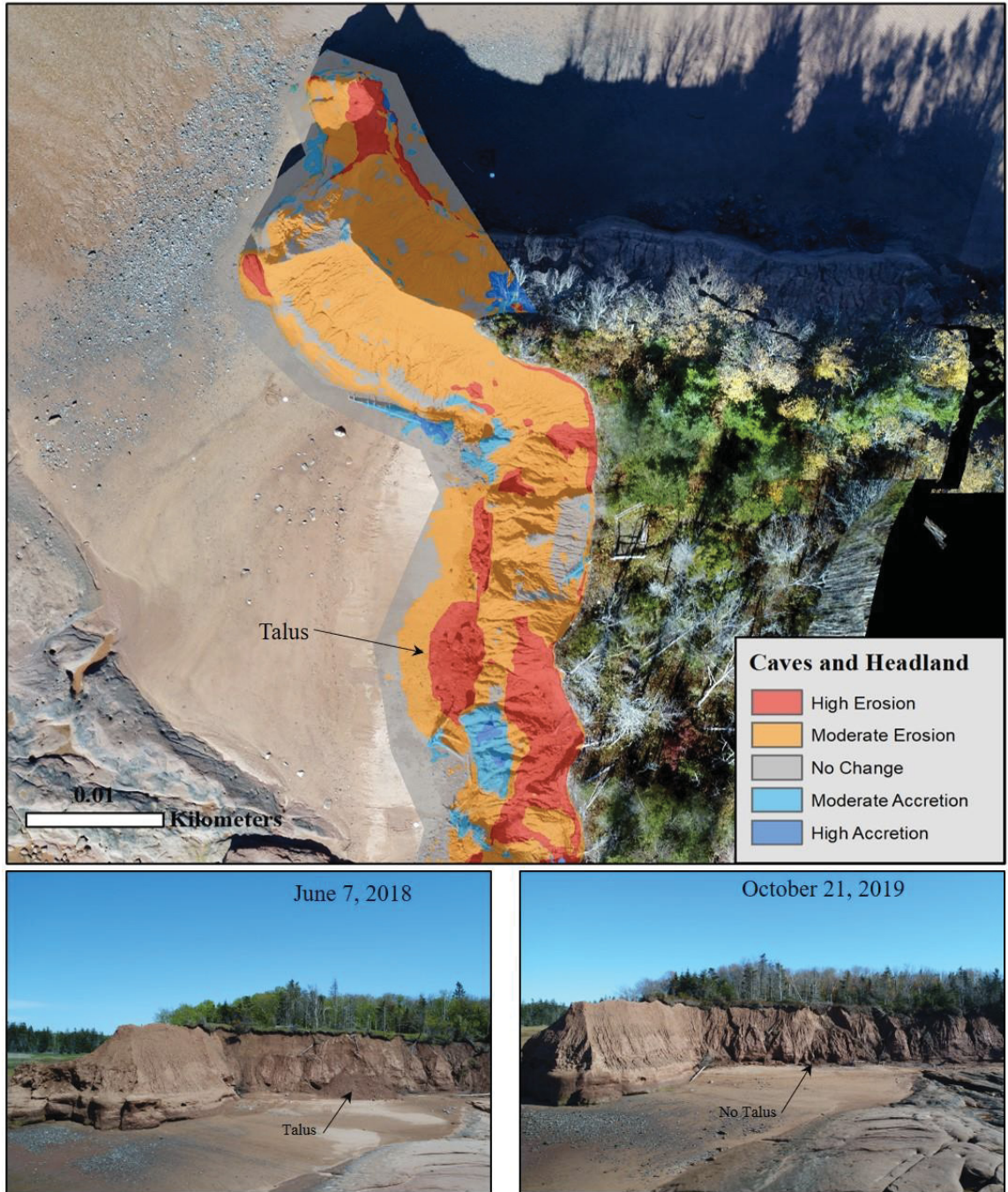
Figure 3.3.3: Vertical change on the cliff face in the vicinity of the Caves and Point study areas between June 7, 2018 and October 21, 2019. A large talus slope of unconsolidated till can be seen clearly in the June 2018 photo, which has been entirely removed by October 2019. Adjacent to the 2018 talus slope, a new pile of material has been deposited from an overlying gully. The deposition of fallen material at the cliff toe and subsequent removal is observed over the course of both study seasons and is likely an annual process.
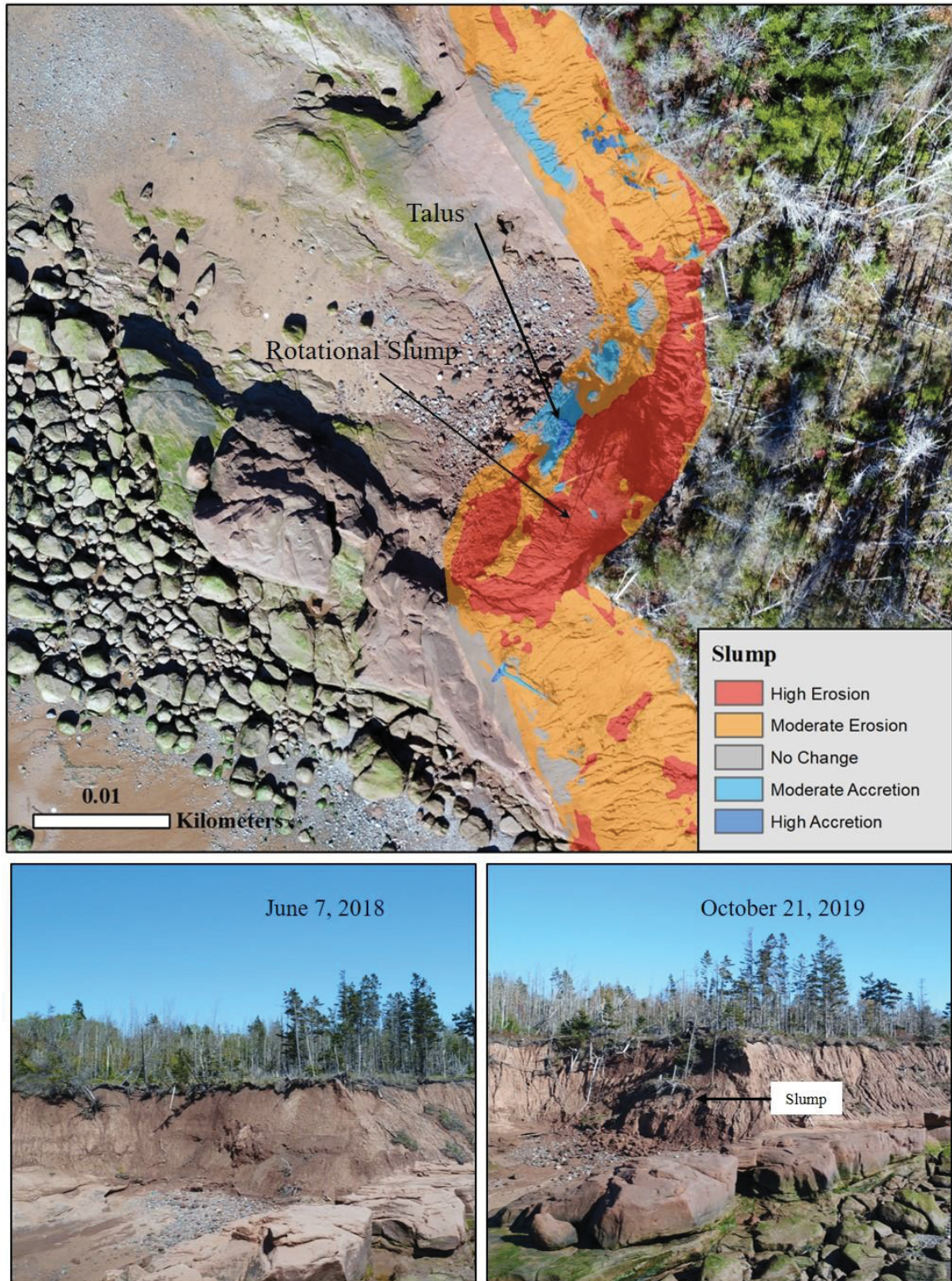
Figure 3.3.4: Vertical change on the cliff face between June 7, 2018 and October 21, 2019 in the vicinity of the Slump study site. A large block of the cliff has broken away from the cliff face and has slumped down. Much of the accreted material at the base of the cliff was likely removed immediately following the main slump event.
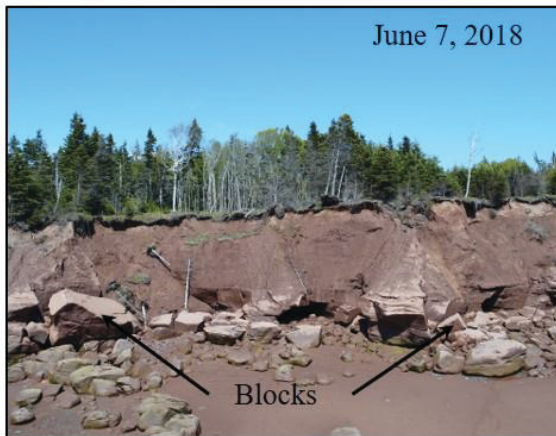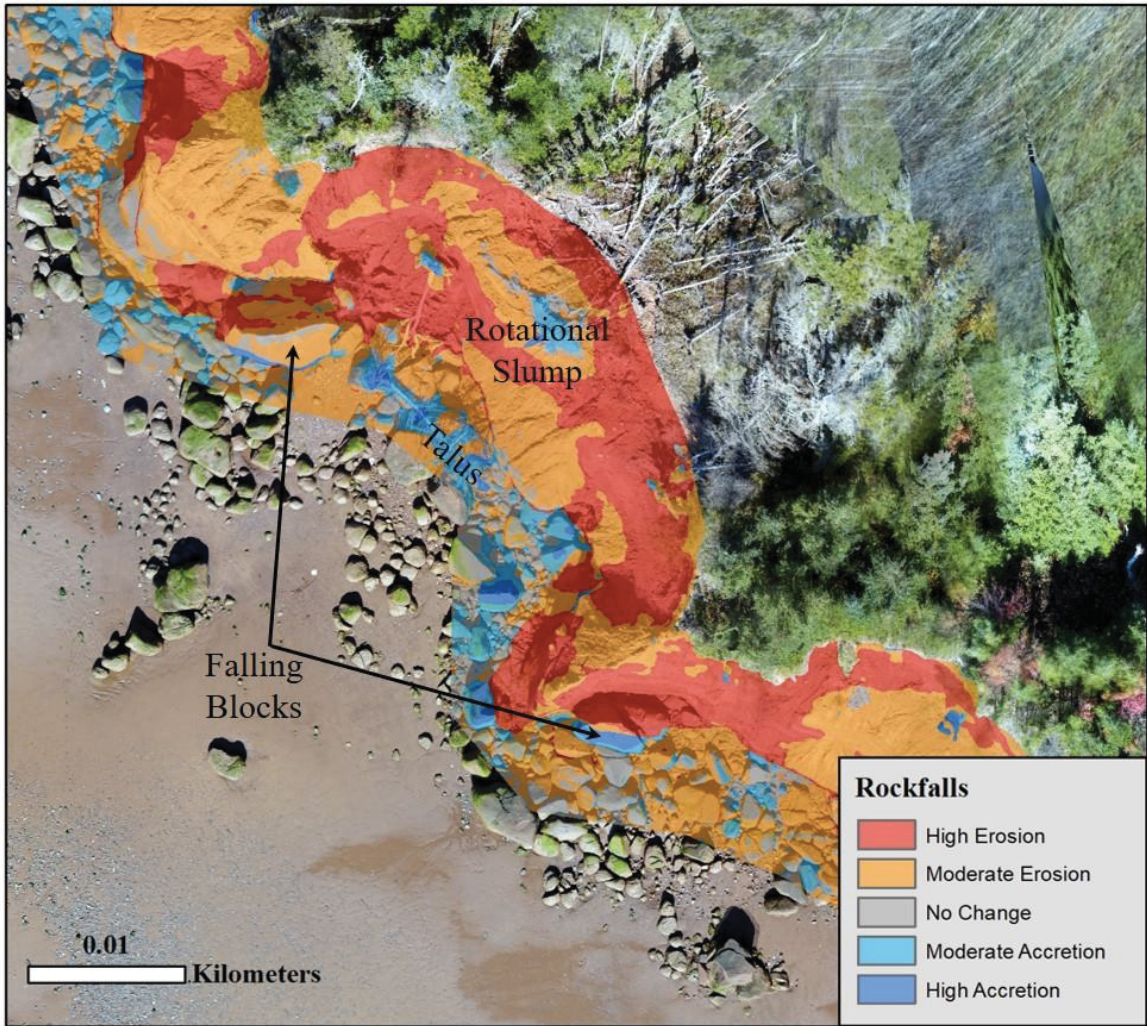
Figure 3.3.5: Vertical change on the cliff face between June 7, 2018 and October 21, 2019 in the vicinity of the Rockfall study area. Two large blocks have become detached from adjacent headlands and are gradually rotating downwards while at the same time breaking into smaller boulders which feed the talus slope below. Rapid retreat in the form of rotational slumping is observed between the two headlands with an associated talus slope at the cliff toe.

3.4 Inundation Frequency

Due to the angle of the bedding surface from which the cliffs rise, the elevation of the cliff toe drops from north to south along the length of the cliff. The elevation of the cliff toe at the Caves and Headland, Slump, and Rockfall sites were compared to pressure sensor data collected between June and October 2019 (Fig. 3.4). The elevation of the pressure sensor was determined using RTK GPS to be -1.308 meters. This value was added to the depth readings to produce corrected values relative to the surveyed CGVD2013 elevation of the sensor. This allowed for comparison of inundation frequency at the elevations of the cliff toe at the Caves and Headlands, Slump, and Rockfall sites.
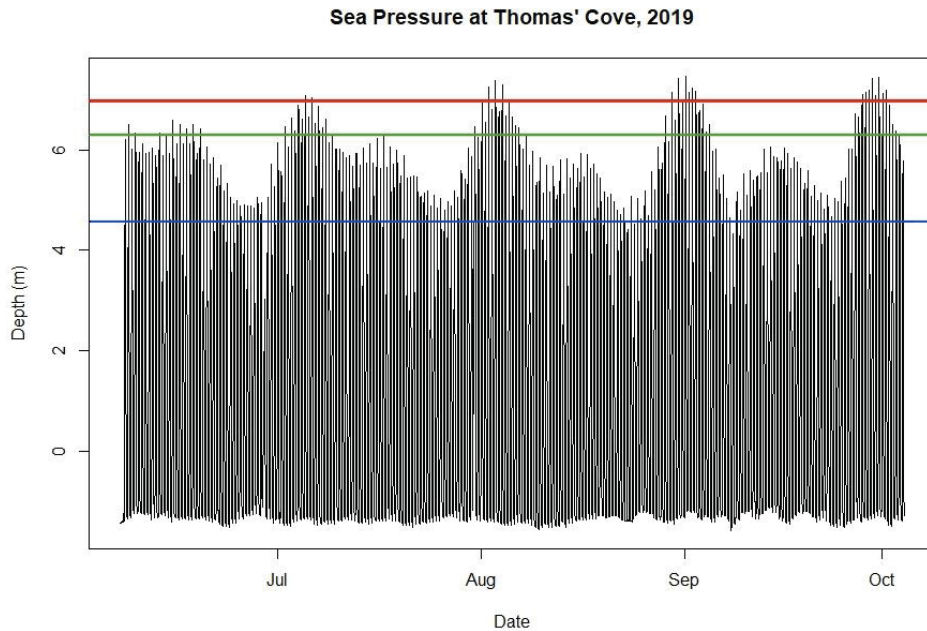
Figure 3.4: Water depth collected by an RBR pressure senor relative to the sensor's vertical position with elevations at the Caves and Headland (red), Slump (green), and Rockfall (blue) shown as horizontal lines.

Comparing cliff toe elevations at the Caves, Slump and Rockfall sites to local pressure sensor data collected between June and September, 2019 reveals that during that period inundation occurs 0.2% of the time the Caves, 1.6% at the Slump, and 18.6% at the Rockfall.

Chapter 4

Discussion:

4.1 Historic Air Photos

Observed retreat rates were largest in the middle of the 20th century. Study of historic air photos showed pronounced decadal changes in coastline morphology, notably the transition from a headlands-dominated coastline in 1948 to one that was more linear, with a few narrow headlands and detached sea stacks by 1972. Large headlands would have disintegrated rapidly as they became detached sea stacks and would have been vulnerable to attack by storms and spring freeze-thaw cycles. Interestingly, three major tropical storms made landfall in the Minas Basin between 1948 and 1954: Hurricane Able in 1950, the Groundhog Day tropical storm of 1952, and Hurricane Carol in 1953. The transition from a headland-dominated shoreline in the 1940s and 1950s to the more linear shoreline seen today is clearly visible in the air photos, is likely responsible for the lower retreat rates observed since 1972 (Fig. 4.1).
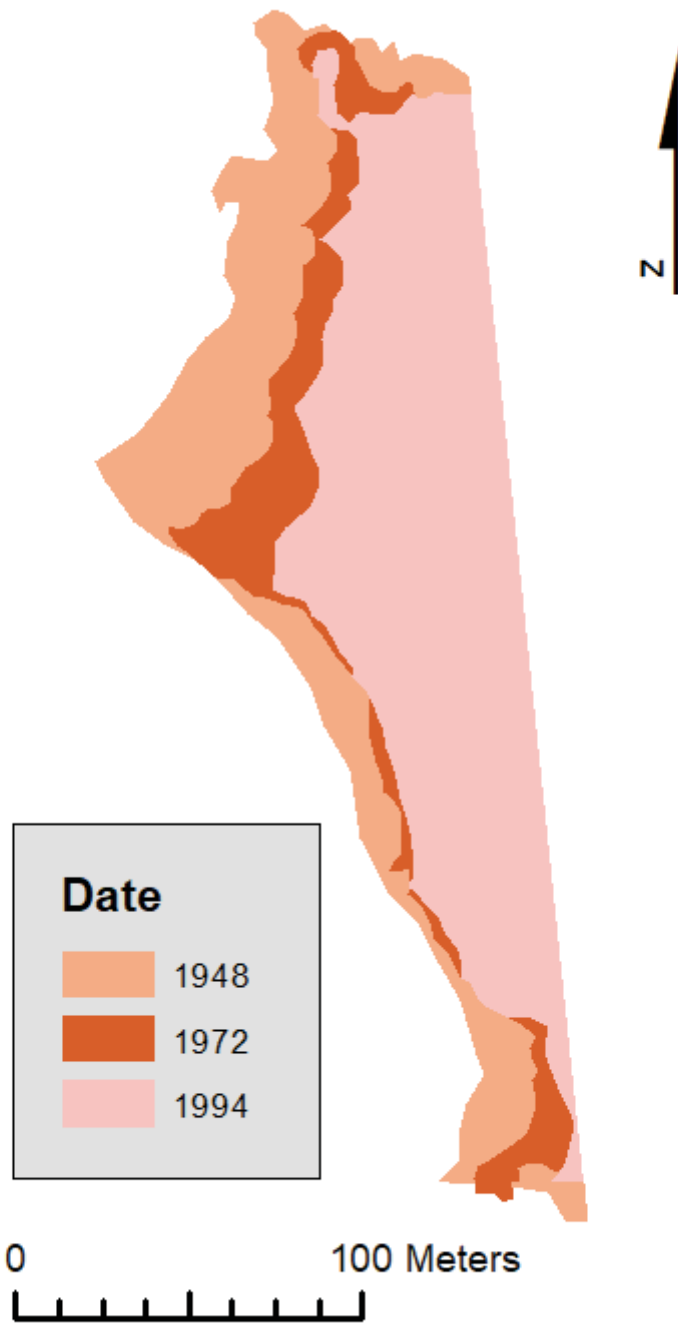
Figure 4.1: Comparison of shorelines in 1948, 1972, and 1994. Large headlands are visible at the north and middle of the cliff. Large headlands have been eroded to narrow spits by 1972 and are significantly smoothed by 1994.

Long-term retreat rates using coastline positions from air photos were consistent with overall retreat values in the same area of coast calculated by Wilson et al., 2017, however, short term retreat values are inconsistent with those found in this study (Table 11).

Table 11: Average retreat rate values (m/yr) reported in Wilson et al., 2017 and this study. Long term retreat from the mid-1900's until present is consistent in both studies but recent short-term retreat is significantly lower in this study.

	Wilson et al., 2017	This Study
1948-2013	NA	0.64
1954-2013	NA	0.41
1964-2013	0.43	NA
1994-2013	0.48	0.25

Wilson et al., 2017 found retreat in the vicinity of Thomas' Cove to be ~0.48 m/yr between 1994 and 2013. However, there exist significant limitations in using historic air photos for analysis of change. Chief among these is the low spatial resolution of historic air photos. The length of pixel edges or the ground sampling distance (GSD), was at best 0.36 m and at worst 0.72 m (Table 2). This means that even under the best circumstances, the GSD is approaching the annual retreat rate. Error was calculated as three times the GSD; the use of air photos is an acceptable practice for long-term, multi-decadal analysis of change, but the magnitude of uncertainty makes estimating decadal retreat rates using air photos less reliable, because the uncertainty for the position of all shorelines is nearly the distance the cliff is expected to move over that decade.

There is also difficulty in performing a quality orthorectification of air photos, and in quantifying the uncertainty associated with the orthorectification. Ideally, the internal triangulation of air photos is corrected before any further georeferencing, but this correction requires the use of fiducial marks located around the perimeter of the air photos, associated metadata such as direction of travel, focal length and camera type, and specialized software (Nikolakopoulos et al., 2019). Air photos provided by the Canadian National Air Photo Library (NAPL) did not include the above information, so the triangulation correction step was not performed. All transformations rely on the accurate placement of ground control points, ideally in an even distribution throughout the frame (Dolan et al., 1991, Bolstad, 2008). Even distribution was not possible using images of Economy Point because one side of the frame was featureless open water. Additionally, land use has changed significantly on Economy Point, meaning that field corners and road intersections that may have been visible in 1938, became overgrown or logged out by the 1950s. The choice to use the affine 1st order polynomial transformation on all air photos was based on its ease of implementation, and the lack of availability of image fiducial marks and metadata. Georectification was not accepted until all field boundaries and roadways were aligned close to the cliff itself, ensuring that corrections were locally acceptable. Higher order polynomial transformations were attempted on select years, but due to the collinearity of the control points, distortion occurred near the edges and around the cliffs in question. By applying an affine 1st order polynomial transformation to all images RMSE values could be compared across all dates.

4.2 Retreat Rates

4.2.1 DSAS

The quality of rate calculations is reflective of the quality of the shorelines used. The statistics generated by DSAS are prone to inaccuracy if transect placement does not allow the cast to pass through all shorelines in question at, or near to right angles. 7-18% of transects were removed due to not being orthogonal to the baseline, which introduced a degree of user-defined variability between dates. Removed transects were concentrated at headlands and therefore the role of headland-dominated erosion was under-represented in these results. Additionally, the problems associated with georeferencing historic air photos discussed above meant that 1938, 1959, 1969, 1979, and 2007 were omitted from analysis altogether.

4.2.2 Historic Retreat

Error likely occurred in attempting to georeference the 1938 air photo. If the position of the resulting shoreline is accurate, the cliff would have to have retreated an average of 34.7 meters over the span of 10 years. Instead of relying upon the 1938 values derived from georectifications performed here, one should instead consider rates that were measured in nearby Upper and Lower Economy between 1938 and 1975 by Atlantic Air Survey Limited, Dartmouth, Nova Scotia reported in Loucks and Porter (1982). Upper Economy was measured having a long-term retreat rate of 0.39 ± 0.02 m/yr while Lower Economy had a retreat rate of 0.26 ± 0.05 m/yr. Loucks and Porter (1982) also performed monthly lot-line surveys to measure episodic retreat rates along the same sections of cliff in 1982 and found that for that year retreat in Upper Economy increased 95% over the

long-term average and Lower Economy increased by 215%. The authors attributed these high retreat rates to 1982 spring thaw. Indeed, by far the highest rates of erosion occurred during April of that year. Although both sites investigated in the report are adjacent to the Thomas' Cove site, and are not entirely exposed headlands, their composition is the same sandstone at Thomas' Cove.

Long-term retreat rates between 1948 and 2013 (-0.56 m/yr), are higher than the long-term rates between 1964 and 1994 (-0.39 m/yr) reported by Wilson et al. (2017) and higher than the retreat rates between 1994 and 2013 (-0.2 m/yr), which indicates that in Thomas' Cove retreat was slower during the period from 1994-2013 relative to the long-term average. However, average retreat between all dates is -0.35 m/yr based on EPR, which is consistent with Wilson et al. (2017).

4.2.3 Modern Retreat

Retreat over the 2018-2019 seasons was faster than long-term rates of retreat from a survey of historic air photos and from coarse estimates made by Wilson et al., 2017. Retreat was on average -0.68 m/yr, based on EPR. For comparison of modern retreat values, this study relies on the findings of time period 2 reported in Wilson, 2016. In area 2 (between Five Islands and Upper Economy) Wilson found that retreat values increased significantly between the first time period (1964 to 1994) to -0.47 m/yr between 1994 and 2013. The rates reported in this study are higher and might suggest that annual retreat rates are increasing from recent historic levels. Continued periodic monitoring of the cliffs at Thomas' Cove should be undertaken to investigate the role of annual variability on long-term retreat rates.

The frequency of retreat events over a single season may not truly reflect modern long-term rates of change (Dolan et al., 1991, Burningham and French, 2017). Moreover, the rates calculated by Wilson are for a broad area, encompassing multiple coastal morphologies that are likely to retreat differently over short time scales. The presence of headlands at Thomas' Cove and the observed high rates of retreat at those headlands would suggest that rates of retreat would be higher for a study focusing at Thomas' Cove than for one which takes the rates of adjacent communities into consideration.

Significant slumping between and at the two headlands at the "Rockfall" site in addition to the ongoing destabilization of the "Slump" site appear to account for the large summertime retreat rates between June and October 2019. However, closer inspection of the cliff break reveals that material has been excavated by early summer leaving a shelf of vegetation overhanging the cliff. This vegetative mat slowly dies and disintegrates over the summer causing retreat rates based on cliff break position to be higher during the summer. The high summertime retreat rates are primarily a lagged artifact of slope failure occurring over the winter and spring.

The central portion of the cliff has a low area which appears to develop into a stream bed that flows east and connects with the small creek that runs into Thomas' Cove. This low area begins near the "Rockfall" site and is easily identifiable from the ground by the large blow-down of trees. These trees were uprooted during several storms in the early spring of 2019 and may be both indicative and the cause of poor soil stability.

Short term retreat values from sRPA imagery provide higher accuracy than decadal or even annual estimates from historic air photos, however the variability associated with the annualized short-term retreat values is much higher. Episodic retreat events have

more influence on annualized rates when short-term measurements are used. Sunamura (2015) shows that for soft rock cliffs as the time interval of cliff recession rates decreases, the standard deviation increases. This may explain the high and wide spread of retreat rates during the June-July 2018 period (Fig. 3.2).

Mis-match in the length of time between surveys makes characterization of seasonal retreat difficult. For example, retreat during 2018 and 2019 summer seasons were statistically similar while the June, 2018 – July, 2018 and June, 2019 – September, 2019 periods were statistically different. This suggests that variability and episodic erosion have a greater influence on short time periods. However, without time periods of similar length from year-to-year, comparison becomes tenuous.

That none of the monthly periods show statistical similarity to the long-term rate of change for the 2018-2019 seasons once again points to high variability associated with short-term rates and suggests that creating an annualized projection of retreat from seasonal data is inappropriate. This is not to say, however, that seasonal and high temporal resolution surveys should not be made, as these are critical for characterizing seasonal retreat between years (if the same time periods are used, as discussed above) and event-driven erosion.

4.2.4 Comparison of historic and modern retreat rates

EPR values observed in the period between 1972 and 1994 were statistically similar to those between 1994 and 2013. This is not in agreement with the findings of Wilson, 2016, who noted a significant increase in erosion rates from time period 1 (1964-1994) to time period 2 (1994-2013), albeit covering a larger geographic area than this study. The

findings of this study suggest that erosion at Thomas' Cove has increased significantly in the past decade compared with rates in the preceding 50 years. Modern erosion rates measured during the 2018-2019 seasons are statistically similar to those between 1954 and 1972. The period from 1954 to 1972 is also the only statistically similar period to the long-term (1948 to 2013) rates. This suggests that erosion at Thomas' Cove may be following a similar pattern now as it was in the mid 1950's to early 1970's. This increased rate of retreat is likely related to a combination of environmental forcings including wave action, freeze-thaw frequency, total precipitation and mean water levels, which work in concert to exacerbate coastal retreat.

4.3 sRPA flights and photogrammetry

In total, 15 sRPA surveys were made at Thomas' Cove between the summer of 2017 and fall of 2019. Of these, only 6 were used for the purposes of this study, due to difficulties in correcting for inappropriately surveyed GCPs, and poor image-quality. Flights carried out on windy days included many blurry images that were unusable in the model. Despite multiple tracks covering the southern end of the cliff, image quality was almost always poor near that end of the study site due to lower image density and for that reason, that end is not included in any of the analysis of change.

The Litchi flight control software was used to create consistent flight paths and standardize survey effort between dates. This software was chosen for compatibility with the Phantom 4 Advanced sRPA. Unfortunately, Litchi failed to allow at-station turns of the aircraft which would have enabled the camera to always be pointed in the direction of travel. Without this, there was no way to adjust for the rolling-shutter affect in photos and a certain degree of distortion exists in all images. Moreover, because the aircraft was

rotating across the transects, the level of distortion is inconsistent between frames, making it difficult to estimate the degree of uncertainty in each image. In the future, the DJI-specific flight controller, DJI GO, which is reportedly capable of executing at-station turns, should be used with a supported aircraft.

It was not until the second season of surveying that the five clifftop GCPs were installed, allowing a back-calculation of the correct position using the two-point localization technique developed in 2019. It may be possible in the future to correct older surveys using natural features such as boreholes and cracks in rock platforms, however for the purposes of this thesis, only the clifftop GCPs were used. For future investigations it is imperative that a reliable network of permanent GCPs be installed as early as possible, ideally before any flight missions are performed.

4.4 Volume contribution

The annual contribution per year per meter of shoreline (m^3/yr/m) recorded in this study (6.79 m^3/yr/m) was consistent with values found in the same region between 1994 and 2013 reported by Wilson et al., 2017 (6.25 m^3/yr/m). The methodology used by Wilson (2016) is sound for estimating long-term volume contributions and has the benefit of requiring no fieldwork. However, short-term volume contributions require the use of the sRPA imagery because uncertainty values associated with shoreline position are much lower than those obtained using air photos which are too high for meaningful volume calculations over a short span of time.

In all volume comparisons, a slight increase in cut volume and total volume was observed from the August 2018 model. This increase likely arose because all volume calculations were based on aligning the polygon with its lowest point and measuring the material above it. Near the end of summer, the cliffs would have contributed less material to the beach surface for a longer duration than other times of year, since freeze-thaw action would have stopped by late spring. As such, material on the beach surface had been removed by tides and currents depressing the elevation of the lowest point in late summer from spring, resulting in a greater total volume within the polygon. Images from August 2018 reveal a slight scarp just in front of the caves and well behind the leading edge of the polygon. Error could also stem from noise within the point cloud, causing the software to wrongly identify the lowest point on the polygon. Visual inspection of the bottom of the August 2018 point cloud revealed that this was not the case in this instance, but it should always be checked moving forward.

Figures 3.3.3-3.3.5 help illustrate where failure is occurring and more importantly where the material lost from the cliff face goes after removal. In Figure 3.3.3, a large talus slope is visible in the June 2018 image which has been almost completely removed by October the following year. Indeed, talus slopes of unconsolidated till such as this were observed to be at their largest in the spring and were largely removed by the end of the summer. This would indicate that material is being lost from the cliff in the winter and spring and is gradually winnowed away by the tides throughout the summer.

Figure 3.3.4 shows the "Slump" site and very clearly illustrates the large rotational slump that occurred between November and December 2018. The cliff break retreated roughly 5 meters during this event and by October 2019 the portion of the clifftop that had

separated was more than half-way down the face of the cliff (~8 meters). Large rotational slumps such as this serve as a significant source of sediment, however unlike the talus slope described above, they will gradually lose material over several seasons as the platform breaks apart and slumps further. After the slumping event the toe was removed and thereby gave way to more slumping. This process is well-documented in literature on coastal and lake bluffs (Himmelstoss et al., 2006, Carter & Guy, 1988).

Finally, Figure 3.3.5 focuses on the vicinity of the "Rockfall" site where two large sandstone blocks have separated from adjacent headlands and have rotated downwards, and in the process broken into smaller boulders which line the toe of the cliff. Failures in stone headlands are most likely the result of freeze-thaw action prying the sandstone apart along already weakened joints. As these large blocks break apart they contribute to the boulder fields that dominate all along the cliff toe.

4.5 Inundation Frequency

The extent of removal is likely related to the inundation frequency at the cliff toe, which is variable along the length of the cliff due to the angle of the bedding plane from which the cliffs rise. The Rockfall site experiences the highest inundation frequency (18.6%) and has a talus slope comprised primarily of large boulders. This is an indication large block failure characteristic of the site as discussed above, but may also point to regular removal of smaller, more mobile material from the cliff toe by frequent inundation. Conversely, the Caves and Headland site is exposed to the lowest inundation frequency (0.15%) and displays a sizeable talus slope of unconsolidated till for much of the year. Removal of this material is highly episodic and must occur during the time when this site

is inundated, either by very high tides or storm events. The variability of talus-slope removal rates along the cliff is related to the degree of protection the talus provides from wave attack, and thereby plays a role in the resiliency of different sections of cliff during storm events through all stages of tide.

4.6 Future work

A longer time series of short-term retreat rates are needed to better constrain the dominant processes responsible for erosion at Thomas' Cove. An on-site monitoring station for water level, rainfall, temperature, wind speed and direction and soil moisture should be installed. Additionally, basic geotechnical properties of the till and sandstone at Thomas' Cove such as hardness and porosity should be measured to allow the site to be better compared to global examples of coastal retreat.

Detailed analysis of the environmental forcings that dominated over the course of this study were not thoroughly investigated and should be considered for improved interpretation in the future. Historic climate records should be compared with decadal retreat rates and air photos to investigate correlation between mass wasting events and periods of increased precipitation, freeze-thaw, and temperature variability. The role of abnormally high water levels and inundation frequency should also be investigated.

A more detailed study of the talus slope and boulder field at the cliff toe is recommended to better constrain the rate at which eroded material from the cliff face becomes mobile sediment. Analysis of grain size distribution using SfM is proposed as a novel approach which can be paired with and validated against traditional geotechnical protocols

This study demonstrates the utility of sRPAs and SfM in estimating volume change in cliffed coastal areas. Expanding this methodology to the rest of the Minas Basin would allow for further comparison of rates estimated by Wilson et al., 2017. By using Thomas' Cove as a test lab, techniques will be refined which will prove useful in filling knowledge gaps in remote sensing of coastal areas already performed by the federal and provincial governments and scientific community. Globally, this methodology could be applied to a wide range of coastal environments, especially where erosion is likely linked to episodic failure events associated with storms or tectonic activity. This technique should be adopted in regions already being monitored by long-term studies of historic air photos as a way of better resolving seasonal mechanisms driving coastline retreat.

Chapter 5

Conclusions:

This study demonstrates that sRPAs can be used for collection of planar and 3D data that allows comparison to historic retreat rate and volume change analysis. Modern retreat rates (1994-2013) from aerial photos are lower than retreat rates between the mid-1950's to early 1970's and are lower than modern short-term retreat measured using SfM. This may be explained by the cliffs now being at a stage of intermediate transition between and headland-dominated shoreline to one that is more linear, as was the case at Thomas' Cove in the 1950s and 60s. Increased retreat may also be explained by locally rising sea levels, which excavate the toe of the cliff faster than in preceding decades and by freeze-thaw frequency and total precipitation. Seasonal variability exists in the form of significantly higher retreat occurring during summer months compared with the rest of the year, which may be caused by a lag in the effects of freeze-thaw action and seasonal removal of material from the cliff toe during this time. Indeed, it appears annual retreat rates are dominated by erosion occurring in the summer, although this is likely a lagged artifact of erosion that actually occurred during the Winter and Spring. The inundation frequency at the cliff toe appears to influence the rate of material removal from the talus slope, which plays a role in armoring the cliff from wave attack during storms.

Volume loss during the 2018-2019 season was consistent with long-term values reported by Wilson (2016), however sRPA imagery has the benefit of lower GSD and hence uncertainty, making short-term estimates of retreat possible.

There are limitations associated with using traditional air photos for calculating rates of coastal retreat in the Minas Basin, chief among those being the inherently high ground

sampling distances, which even under the best circumstances approach the estimated rates of annual retreat for the area. Structure-from-Motion on sRPA-derived imagery offers an order of magnitude higher accuracy alternative which can be performed more frequently and at lower cost than either air photo or LiDAR collection missions.

Coastal erosion serves as a major source of sediment to the coastal ocean. This study found that volume change calculations performed on 3D point clouds were not significantly different from the annual volume contributions calculated by Wilson (2016). This validates the robustness of the technique and shows that it may continue to be used as a fully remote, low-cost method of monitoring sediment contributions from coastal cliffs.

Retreat rates calculated for the 2018-2019 seasons were higher than those reported by Wilson et al., 2017 for the period between 1994 and 2013 but may not be reflective of current long-term trends. For this reason, it is advised that the techniques described in this study be applied to future years at Thomas' Cove and throughout the Minas Basin, as the adoption of sRPA technology will greatly enhance the understanding of coastal change in this region and will complement ongoing monitoring techniques.

References:

Amos, C.L., Long, B.F.N., (1980) *The sedimentary character of the Minas Basin, Nova Scotia.* In The Coastline of Canada, Edited by McCann, B.S. Geological Survey of Canada, pp. 123-152.

Ancilliotto, L., Rydell, J., Nardone, V., Russo, D. (2014) *Coastal cliffs on islands as foraging habitat for bats.* Acta Chiropteroligica. 16. 1, 103-108.

Bolstad, P. (2008) *Chapter 4: Maps and Data Entry.* GIS Fundamentals: A First Text on Geographic Information Systems. 3rd edition. University of Minnesota, St. Paul. 123-174.

Brooks, S.M., Spencer, T. (2010) *Temporal and spatial mechanisms in recession rates and sediment release from soft rock cliffs, Suffolk coast.* UK Geomorphology. 124: 26-41.

Brown, S., Nicholls, R.J., Hanson, S., Brundrit, G., Dearing, J.A., Dickson, M.E., Gallop, S.L., Gao, S., Haigh, I.D., Hinkel, J., Jiménez, J.A. (2014) *Shifting persectives on coastal impacts and adaptation.* Nature Climate Change. 4. 752.

Burningham, H., French, J. (2017) *Understanding coastal change using shoreline trend analysis supported by cluster-based segmentation.* Geomorphology. 282, 131-149.

Caroti, G., Zaragoza, I.M.E, Piemonte, A. (2015*) Accuracy assessment in Structure-from-Motion 3D construction from UAV-born images: the influence of the data processing methods.* International Archives of the Photogrammetry, Remote Sensing and Spatial Information Sciences, V XL-1/W4.

Carter, C. H., Guy, D.E., (1988) *Coastal erosion: Processes, timing and magnitudes at the bluff toe.* Marine Geology. 84, Iss. 1-2. 1-17.

Colwell, J.A., Ferguson, S.A., (1992) *Geology of the Horton Bluff Formation at blue beach*.   Prepared for the Geological Association of Canada and Mineralogical

Association of Canada Joint Annual Meeting in Wolfville, Nova Scotia. May 25-27, 1992; meeting hosted by the Atlantic Geoscience Society. Available online: http://ees.acadiau.ca/ft1.html. Accessed: October 5th, 2017.

Cooper, A. (1997) *Plant species coexistence in cliff habitats.* Journal of Biogeography. 24, 483-494.

Dolan, R., Fenster, M.S., Holme, S.J. (1991) *Temporal Analysis of Shoreline Recession and Accretion.* Journal of Coastal Research. 7:3, 723-744.

Dupont, F., Hannah, C.G., Greenberg, D.A., Cherniawsky, J.Y., and Namie, C.E. (2002) *Modelling System for Tides.* Canadian Tech. Rep. Hydrogr. Ocean Sci. 221:vii, 72 pp.

Dupont, Frédéric, Charles G. Hannah and David Greenberg. 2003. *Modelling the Sea Level in the Upper Bay of Fundy.* Atmos.-Ocean. 43(1), 33-47.

Emery, K.O., Kuhn, G.G. (1982) *Sea cliffs: their processes, profiles, and classification.* Geological Society of America Bulletin. 93: 644-654.

Greenberg, D.A., Blanchard, W., Smith, B., Barrow, E. (2012) *Climate Change, Mean Sea Level, and High Tides in the Bay of Fundy.* Atmosphere-Ocean, 50:3, 261-276.

Himmelstoss, E., FitzGerald, D., Rosen, P., Allen, J., (2006) *Bluff evolution along coastal drumlins: Boston Harbor Islands, Massachusetts.* Journal of Coastal Research. 22. 5, 1230-1240.

Himmelstoss, E., Henderson, R.E., Kratzmann, M.G., Farris, A.S. (2018) *Digital Shoreline Analysis System (DSAS) Version 5.0 User Guide.* U.S. Geological Survey Open-File Report 2018-1179, 110 p.

Kam, K. (2018) *Terrestrial and oceanographic forcing of Seacliff erosion in Minas Basin and the assessment of an erosion even using Structure-from-Motion in Economy, Nova Scotia.* Honors thesis. Department of Oceanography, Dalhousie University, Halifax, NS.

Kettanah, Y.A., M.Y. Kettanah, and G.D. Wach. (2013) *Provenance, diagenesis and reservoir quality of the Upper Triassic Wolfville Formation, Bay of Fundy, Nova Scotia, Canada*. Geological Society of London: Special Publications, 417.

Lague, D., Brodu, N., Leroux, J. (2013) *Accurate 3D comparison of complex topography with terrestrial laser scanner: application to the Rangitikei canyon (N-Z)*. ISPRS Journal of Photogrammetry and Remote Sensing. 82.

Louks Oceanography Ltd., Porter and Associates Ltd., (1982) *Erosion and Shore Protection Study*. Nova Scotia Department of The Environment.

Mancini, F., Dubbini, M., Gattelli, M., Stecchi, F., Fabbri, S., Gabbianelli, G. (2013) *Using unmanned aerial vehicles (UAV) for high-resolution reconstruction of topography: the structure-from-motion approach on coastal environments*. Remote Sensing. 5. 6880-6898.

Marques, F., Matildes, R., Redweik, P. (2011) *Statistically based sea cliff instability hazard assessment of Burgau-Lagos coastal section (Algarve, Portugal)*. Journal of Coastal Research. 64. 927-931.

Maxouris, C. (2019) *"Three people were killed after a cliff collapsed on an Encinitas beach"*. Cable News Network. August 3, 2019.

McCorquodale, D. Banks, D., Kerr, M., Knapton, R., Harris, D. (2004) *Changes in the populations of nesting seabirds in the Bird Islands, Cape Breton, Nova Scotia*. Proceedings of the Nova Scotia Institute of Science. 42. 2, 241-252.

Micheletti, N., Chandler, J.H., Lane, S. (2015) *Structure from Motion (SfM) Photogrammetry*. British Society for Geomorphology. Geomorphological Techniques, Chap. 2 Sec. 2.2.

O'Reilly, C.T.R.; Ron Solvason and Christian Solomon (2005). "Where are the World's Largest Tides". In Ryan, J. BIO Annual Report "2004 in Review" (in English) (Washington, D.C.: Biotechnol. Ind. Org.): 44-46.

Paone, L., Catto, N., Forbes, D.L., and Liverman, D., (2003). Coastal hazard vulnerability, Conception Bay South -Holyrood, NL: impacts and adaptations to climate variability. Paper presented at the Joint Annual Meeting of the Canadian Quaternary Association and the Canadian Geomorphology Research Group, Halifax, Nova Scotia, June 8-12, 2003.

Parker, M., M. Westhead, and A. Service, (2007). *Ecosystem overview report for the Minas Basin Nova Scotia*. Prepared for Ocean and Habitat Branch Maritimes Region, Fisheries and Oceans Canada.

Prosdocimi, M., Calligaro, S., Sofia, G., Dalla Fontana, G., Tarolli, P. (2015) *Bank erosion in agricultural drainage networks: new challenges from structure-from-motion photogrammetry for post-event analysis.* Earth Surface Processes and Landforms. 40, 1891-1906.

Ruzic, I., Marovic, I., Benac, C., Ilic, S., (2014). *Coastal cliff geometry derived from structure-from-motion photogrammetry at Stara Baska, Krk Island, Croatia*. Geo-Marine Letters. 34, Issue 6, pp. 555-565.

Shürch, P., Densmore, A.L., Rosser, N.J., Lim, M., McArdell, B.W. (2011) *Detection of surface change in complex topography using terrestrial laser scanning: application to the illgraben debris-flow channel.* Earth Surface Processes and Landforms. 36, Issue 14, 1847-1859.

Spooner, Ian & Batterson, Martin & Catto, Norm & Liverman, David & E. Broster, Bruce & Kearns, Kim & Isenor, Fenton & Wayne Mcaskill, G. (2012). Slope failure hazard in Canada's Atlantic Provinces: A review. Atlantic Geology. 49. 1-14. 10.4138/atlgeol.2013.001.

Statistics Canada. (2017) *Cumberland, Subd. A, Nova Scotia and Canada. Census Profile. 2016 Census*. Statistics Canada Catalogue no. 98-316-X2016001. Ottawa. Released September 13, 2017. http://www12.statcan.gc.ca/census-recensement/2016/dp-pd/prof/index.cfm?Lang=E. Accesed October 6, 2017.

Stavrou, A., Lawrence, J.A., Mortimore, R.N., Murphy, W., (2011) *A geotechnical and GIS based method for evaluating risk exposition along coastal cliff environments: a case study of the chalk cliffs of southern England. Natural Hazards and Earth System Sciences*. Katlenburg-Lindau. 11.11 (2011): 2997.

Sunamura, T. (2015) *Rocky coast processes: with special reference to the recession of soft rock cliffs*. Proceedings of the Japanese Academy. B 91.

Trenhaile, A., (2016) *Rocky coasts – their role as depositional environments*. Earth Science Reviews. 159; 1-13.

Warrick, J., Ritchie, A., Adelman, G., Adelman, K., Limber., P., (2017). *New techniques to measure cliff change from historical oblique aerial photographs and structure-from-motion photogrammetry*. Journal of Coastal Research; Fort Lauderdale. 33.1: pp. 39-55.

Willcocks-Musselman, R., (2003*) Minas Basin Watershed Profile, Report 2*, Bay of Fundy Ecosystem Partnership, Acadia University, Wolfville, NS.

Wilson, E., (2016) *An assessment of coastal erosion in the Minas Basin, Nova Scotia*. MSc thesis. Department of Oceanography. Dalhousie University, Halifax, NS.

Wilson, E.K., Hill, P.S., van Proodij, D., Ruhl, M., (2017) *Coastal retreat rates and sediment input to the Minas Basin, Nova Scotia*. *Canadian Journal of Earth Sciences*: 54. 370-378.

Wisconsin Department of Transportation (2017) *Surveying and Mapping – Real Time Kinematic (RTK) Surveys*. Facilities Development Manual. 2020. pp. 1-23.

Wong, P.P., Losada, I.J., Gattuso, J.-P., Hinkel, Khattabi, J., A., McInnes, K.L., Saito, Y., and Sallenger, A. (2014) *Coastal systems and low-lying areas*. In: Climate Change 2014: Impacts,Adaptation, and Vulnerability. Part A: Global and Sectoral Aspects. Contribution of Working Group II to the Fifth Assessment Report of the Intergovernmental Panel on Climate Change [Field, C.B., V.R. Barros, D.J. Dokken, K.J. Mach, M.D. Mastrandrea, T.E. Bilir, M. Chatterjee, K.L. Ebi, Y.O. Estrada, R.C. Genova, B. Girma, E.S. Kissel, A.N. Levy, S. MacCracken, P.R. Mastrandrea, and L.L.White (eds.)]. Cambridge University Press, Cambridge, United Kingdom and New York, NY, USA, pp. 361-409.

Young, A.P, Carilli, J.E., (2018) *Global distribution of coastal cliffs*. Earth surface Processes and Landforms. 44, 1309-1316.